A multi-temporal and multi-angular approach for systematically retrieving soil moisture and vegetation optical depth from SMOS data

Yu Bai, Tianjie Zhao, Li Jia, Michael Cosh, Jiancheng Shi, Zhiqing Peng, Xiaojun Li, Wigneron J.-P.

Remote Sensing of Environment 280 (2022) 113190

Contents lists available at ScienceDirect

Remote Sensing of Environment

journal homepage: www.elsevier.com/locate/rse

A multi-temporal and multi-angular approach for systematically retrieving soil moisture and vegetation optical depth from SMOS data

Yu Bai [a,b], Tianjie Zhao [a,*], Li Jia [a,*], Michael H. Cosh [c], Jiancheng Shi [d], Zhiqing Peng [a,b], Xiaojun Li [e], Jean-Pierre Wigneron [e]

[a] State Key Laboratory of Remote Sensing Science, Aerospace Information Research Institute, Chinese Academy of Sciences, China
[b] University of Chinese Academy of Sciences, China
[c] USDA-ARS Hydrology and Remote Sensing Laboratory, United States of America
[d] National Space Science Center, Chinese Academy of Sciences, China
[e] INRAE, UMR1391 ISPA, F-33140, Villenave d'Ornon, France

ARTICLE INFO

Edited by Jing M. Chen

Keywords:
SMOS
Soil moisture
Vegetation optical depth
Surface roughness
Multi-temporal
Multi-angular

ABSTRACT

Passive microwave remote sensing of soil moisture is an underdetermined problem, as observed microwave emission from the landscape is affected by a variety of unknown surface parameters. Increasing observation information is an effective means to make retrievals more robust. In this study, a multi-temporal and multi-angular (MTMA) approach is proposed using SMOS (Soil Moisture and Ocean Salinity) satellite L-band data for retrieving vegetation optical depth (VOD_p, p indicates the polarization with H for horizontal and V for vertical)), effective scattering albedo (ω_p^{eff}), soil surface roughness (Z_p^s), and soil moisture (SM_p). The advantage of the MTMA approach is that it does not need auxiliary data as inputs or constraints. SMOS polarization-dependent VOD are produced and compared at a global scale for the first time, and it is found that the polarization difference of vegetation effects should not be ignored in the SM retrieval algorithm. The MTMA VOD retrievals are found to have a reasonable global spatial distribution, which is generally consistent with the VOD retrievals obtained from the SMOS Level 3 (SMOS-L3) and SMOS-IC Version 2 (V2) (referred to as SMOS-IC), except for showing relatively lower values over densely vegetated areas compared with the other two SMOS products. The spatial distribution of retrieved ω_p^{eff} generally shows a dependence on both VOD and land cover types. In addition, the values of *MTMA*-ω_V^{eff} are higher than that of *MTMA*-ω_H^{eff}, indicating stronger microwave scattering of V-pol in the vegetation layer than that of H-pol. The retrieved surface roughness parameter (Z_p^s) ranges from 0.04 to 0.22 cm, and its spatial distribution is partially different from the existing roughness products/auxiliary data from SMOS and SMAP. The retrieved MTMA SM shows generally high correlations with in-situ measurements (11 dense observation networks) with overall correlation coefficients of > 0.75. The overall ubRMSE of *MTMA*-SM_H and *MTMA*-SM_V are < 0.055 m^3/m^3 and lower than that of SMOS-IC and SMOS-L3 products. SMOS-IC generally presents higher correlation coefficients compared to MTMA in most sites outside China; in China, RFI filtering is crucial and makes it very difficult when comparing algorithms based on different brightness temperature products. The number of effective retrievals of *MTMA*-SM_H and MTMA-SM_V ranges from 1409 to 1640 and 1104 to 1603 respectively, which is more than that from SMOS-IC (from 236 to 1358) over the selected 11 networks. Therefore, it is concluded that by incorporating multi-temporal SMOS data, the proposed method of MTMA can be used to systematically retrieve SM, VOD and additional surface parameters (effective scattering albedo and surface roughness) with comparable or better performance of SM than that of SMOS-IC and SMOS-L3. Moreover, this paper for the first time produced a polarization-dependent SMOS VOD product at a global scale.

* Corresponding authors at: State Key Laboratory of Remote Sensing Science, Aerospace Information Research Institute, Chinese Academy of Sciences, Beijing 100101, China.
E-mail addresses: zhaotj@aircas.ac.cn (T. Zhao), jiali@aircas.ac.cn (L. Jia).

https://doi.org/10.1016/j.rse.2022.113190
Received 20 June 2022; Accepted 19 July 2022
Available online 13 August 2022

1. Introduction

Surface soil moisture (SM) usually refers to the soil moisture in the upper soil layer of 0–5 cm, and plays a key role in governing the exchanges of water and energy between the land and the atmosphere. Accurate estimation of SM is required for many studies, such as agricultural productivity forecasts, flood and drought monitoring, regional water resources management, and the global water cycle (Seneviratne et al., 2010; Zhao et al., 2020b).

Currently, microwave L-band radiometer is considered an appropriate tool for spatial SM mapping from space due to its strong penetration of vegetation covers and sensitivity to surface SM conditions (Kerr et al., 2001). Satellites with L-band radiometer mainly include the Soil Moisture Active Passive (SMAP) from National Aeronautics and Space Administration (NASA) of the United States of America (USA), SMOS from European Space Agency (ESA) and Aquarius/SAC-D (Satélite de Aplicaciones Científicas D) from the joint efforts by NASA and CONAE (Comisión Nacional de Actividades Espaciales) of Argentina. Moreover, the Copernicus Imaging Microwave Radiometer (CMIR) mission (Kilic et al., 2018) and the China's Terrestrial Water Resources Satellite (TWRS) (Zhao et al., 2020b) may bring continuity to microwave L-band radiometry from space. Launched by the ESA in 2009, SMOS was the first satellite to operate with a L-band (1.4 GHz) radiometer. SMOS acquires multi-angular brightness temperature (TB) globally with a spatial resolution of approximately 43 km. Currently, there are two global SM products provided routinely based on SMOS observations, i.e., the SMOS products released by the Centre Aval de Traitement des Données (CATDS) (referred to as SMOS-Level 2 (L2)/Level 3 (L3)) and SMOS-IC V2 (version 2) product released by INRAE (l'Institut national de recherche pour l'agriculture, l'alimentation et l'environnement). The multi-angular retrieval algorithms of SMOS L2 (Kerr et al., 2012) and L3 (Al Bitar et al., 2017) SM products are all based on the forward model of L-band Microwave Emission of the Biosphere (L-MEB) (Wigneron et al., 2007), and both SM and VOD are simultaneously retrieved with empirical and static model parameters (Wigneron et al., 2021). Numerous validation/evaluation studies of SMOS L2/L3 SM products have been carried out during the last decade and some of them show that the SMOS L2/L3 SM products might present underestimation when compared with ground measurements (Gherboudj et al., 2012; Peng et al., 2015; Chen et al., 2017; Wigneron et al., 2017). The underestimations may be partially attributed to the sun glint and the radio frequency interference (RFI) which increases the observed TB, and partially attributed to the SM retrieval algorithm, e.g., the VOD retrieved by the SMOS L2/L3 algorithm was found to be relatively noisy (Grant et al., 2012; Zhao, 2018), and thus leading to corresponding uncertainties in SM retrievals (Jackson et al., 2012; Schlenz et al., 2012; Chen et al., 2017).

Considering the above mentioned issues, the SMOS-IC algorithm was developed by the activities funded by ESA- and CNES (Centre national d'études spatiales) aiming at improving SMOS algorithms (Fernandez-Moran et al., 2017a; Wigneron et al., 2021). In contrast to the SMOS L2/L3 algorithms, the SMOS-IC algorithm assumes that the pixels are homogeneous and thus becomes independent of the ECMWF (European Centre for Medium-Range Weather Forecasts) SM information, which has to be used as auxiliary information for forward model simulations in the subordinate pixel fractions of heterogeneous pixels in the SMOS L2/L3 algorithms (Li et al., 2020); SMOS-IC uses SMOS-L3 TB data at fixed view-angle ranging from 20° to 55° ± 2.5° and does not consider corrections of the antenna pattern and the complex SMOS viewing angle geometry (Ebrahimi-Khusfi et al., 2018). Furthermore, new empirical but static parameters of effective scattering albedo (ω_p^{eff}), which describes the vegetation scattering effects and soil roughness, are implemented in SMOS-IC by calibrating the L-MEB model for different IGBP land cover types (Fernandez-Moran et al., 2017b) based on a global map of soil roughness (Parrens et al., 2016). Although the SMOS-IC SM and VOD products performed very well compared with those of SMOS L2/L3 (Fernandez-Moran et al., 2017a; Ebrahimi-Khusfi et al., 2018; Rodríguez-Fernández et al., 2018; Tian et al., 2018; Al-Yaari et al., 2019; Wigneron et al., 2021), it was found that the SMOS-IC SM product could still be improved (Diego et al., 2018; Li et al., 2020), since those model parameters are arbitrarily assumed to be constant in time and independent on the incident angle and polarization (Griend and Owe, 1994; Kerr et al., 2012; Fernandez-Moran et al., 2017a). For example, the new SMOS-IC V2 retrieval algorithm introduces the average VOD values from previous days as the initial value of VOD for subsequent retrievals, instead of using average VOD values over the years to initialize VOD (Wigneron et al., 2021).

Both the SMOS L2/L3 and SMOS-IC algorithms are based on fixed empirical/theoretical parameters of ω_p^{eff} and soil roughness. However, ω_p^{eff} not only depends on the land cover types with associated errors but also varies for the same vegetation type (Konings et al., 2016; 2017). Kurum (2013) found that ω_p^{eff} showed significant polarization dependence for specific vegetation types and Wigneron et al. (2004a) found that both the temporal and polarization variations of ω_p^{eff} were significant over crop fields. Zhao et al. (2020a) showed that the optimized ω_p^{eff} depended on both incidence angle and polarization at L-band. In addition, Davenport et al. (2005) and Fernandez-Moran et al. (2017b) confirmed that errors in ω_p^{eff} could increase the uncertainties in the retrievals of SM and VOD, because the dependence of ω_p^{eff} on polarization and its variation over time were not fully considered in the current implementation of the SMOS L2/L3 and SMOS-IC SM retrieval algorithms, and even not in the SMAP algorithms.

Another parameter that reflects the impact of vegetation is VOD, which depends on time, polarization, frequency, vegetation water content, vegetation structure, etc. (Wigneron et al., 1995; Wigneron et al., 2004a; Konings et al., 2021). The vegetation layer not only emits microwave radiation, but also attenuates the microwave radiation of the soil layer. When the thickness of vegetation layer increases, it may even lead to the failure of the soil layer signal to break through the vegetation layer, thus affect the retrieval of soil moisture. Wigneron et al. (1995) considered VOD was polarization dependent and introduced the C_p parameter to account for such effect. This polarization dependence was also analyzed in Wigneron et al. (2004a). Konings et al. (2021) also argued that in view of the large variations of vegetation water content (i.e., VOD is the function of vegetation water content) within different vegetation components or types, the polarization dependence should be considered in the SM retrieval algorithm, otherwise it would cause the uncertainty and insufficient understanding of VOD retrievals.

Soil roughness also affects the microwave emission of land surface, and the roughness effects vary with frequencies, angles of incidence and polarizations (Wigneron et al., 2011; Montpetit et al., 2015; Zhao et al., 2015a; Parrens et al., 2016; Peng et al., 2017; Wigneron et al., 2017). The roughness model used in SMOS L2/L3 and SMOS-IC is a semi-empirical model, in which the roughness effects are characterized by three parameters, i.e. the polarization mixing factor (Q^r), parameter H^r and N_p^r (H^r describes influences of both geometric roughness and dielectric roughness, N_V^r, and N_H^r describes angular effects) (Lawrence et al., 2013). Many studies have described the optimization of these roughness parameters under different surface conditions (Parrens et al., 2016; Al Bitar et al., 2017; Wigneron et al., 2017). The roughness parameters in the SMOS L2/L3 and SMOS-IC algorithms are assumed to be time-invariant. However, the soil roughness varies with time due to wind erosion, rainfall, irrigation and farming, etc.. Parrens et al. (2016) and Chaubell et al. (2020) demonstrated that the SM retrievals could be improved by using optimized surface roughness parameters.

As a summary, effective scattering albedo and soil roughness have direct impacts on the retrievals of SM and VOD. However, their variation with time and the polarization-related properties of the retrievals are poorly understood. To fill this gap and further improve the performance of the SM and VOD retrievals using the SMOS data, a multi-temporal and multi-angular approach, MTMA, is proposed in this paper to systematically retrieve four parameters including VOD, SM, effective scattering

Table 1
Information of the datasets used in this study

Variable name	Product name	Spatial (gridded) resolution	Temporal resolution	Unit	Download address
TB	SMOS L1C	15 km	Daily	K	smos-diss.eo.esa.int
	SMOS L3	25 km	Daily	K	http://www.catds.fr/
SM and VOD	SMOS L3	25 km	Daily	SM (m^3/m^3) VOD (no unit)	http://www.catds.fr/
	SMOS-IC	25 km	Daily	SM (m^3/m^3) VOD (no unit)	https://ib.remote-sensing.inrae.fr/
NDVI (MOD13C1)	MODIS	0.05°	16 days	–	https://search.earthdata.nasa.gov/
AGB	ESA CCI	100 m	–	mg/ ha	http://cci.esa.int/biomass/
soil roughness (h)	SMAP SCA	9 km	–	cm	https://nsidc.org/data/SMAP/
	SMAP DCA	9 km	–	cm	https://nsidc.org/data/SMAP/
	SMOS	25 km	–	cm	http://www.catds.fr/
soil temperature and precipitation	ECMWF	15 km	Daily	Soil temperature (K) Precipitation (mm)	smos-diss.eo.esa.int

albedo and surface roughness. The multi-temporal approach, which assumes that the vegetation does not change in temporal adjacent overpasses, has been previously used to increase the independent information used as input in the retrieval algorithms and thus improve the capabilities of the retrieval algorithms (Wigneron et al., 2000; Konings et al., 2016; Konings et al., 2017; Li et al., 2021a; Li et al., 2022). In this study, the SMOS V-pol MVIs was proposed based on the SMOS H-polarized microwave vegetation indices (MVIs) (Cui et al., 2015), in which only VOD was retrieved through three pairs of TBs at (30°, 40°), (35°, 45°) and (40°, 50°). The MTMA approach developed in this study is a further development of the multi-angular approach based on the SMOS MVIs by Cui et al. (2015). The adoption of a combined multi-angular and multi-temporal/orbital information is expected to increase the robustness of the VOD and SM retrievals and make the systematic retrievals of effective scattering albedo and soil roughness possibly with more independent information incorporated as inputs in the retrieval algorithm. Therefore, the method proposed in the study would be more suitable for the retrievals of SM and VOD at the global scale.

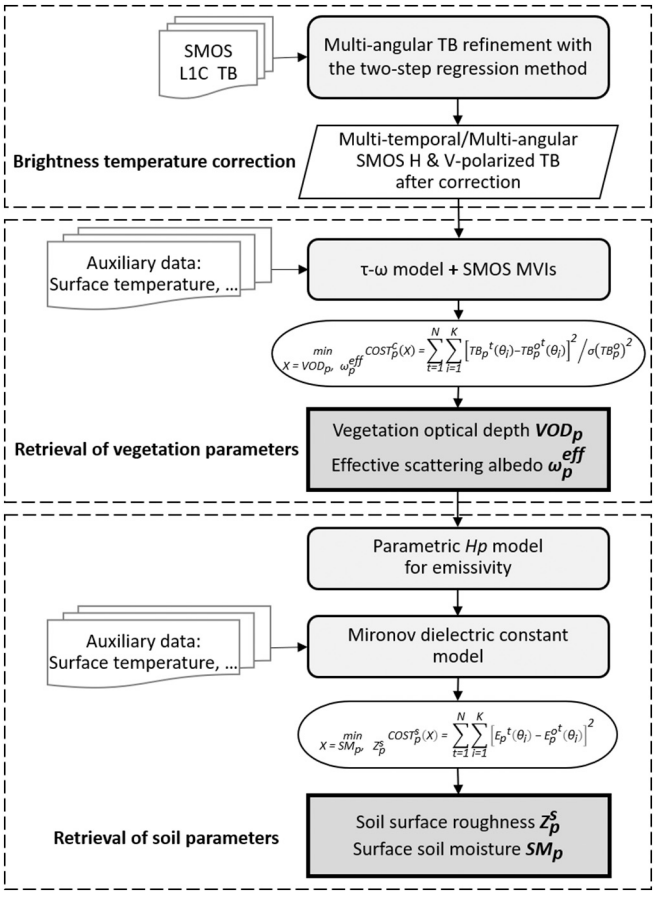

Fig. 1. Flow chart of the multi-temporal and multi-angular approach for systematically retrieving VOD_p, ω_p^{eff}, SM_p and Z_p^s.

The proposed MTMA method presented in this study is different from the SMOS and SMOS-IC algorithms in several aspects and the main ones are: (1) four parameters (vegetation optical depth VOD_p, effective scattering albedo ω_p^{eff}, soil surface roughness Z_p^s, and surface soil moisture SM_p) are retrieved systematically; (2) vegetation parameters (VOD_p and ω_p^{eff}) and soil parameters (SM_p and Z_p^s) are retrieved in two physically separated steps to reduce the uncertainties due to the mutual coupling of the vegetation and soil information; (3) the proposed MTMA algorithm is implemented with the use of single polarization observation instead of using two polarizations that commonly ignore the polarization dependence of vegetation effects; (4) a parametric H_p model (Zhao et al., 2015a), which describes the complex roughness effects depending on incidence angle and polarization, is used to retrieve SM and surface roughness.

The detailed description of the method is given in the following sections.

2. Data and pre-processing

2.1. Satellite products and auxiliary data

In this study, the refined SMOS Level 1C (SMOS L1C) and the original Level 3 (L3) TB data are applied to the MTMA algorithm for retrievals. The VOD and SM from SMOS-IC V2 and SMOS L3 products are used for inter-comparison. The auxiliary data, including the MODIS NDVI product (MOD13C1), the ESA CCI aboveground biomass (AGB), soil roughness (h) products/ancillary and the ECMWF precipitation data are used to evaluate the MTMA performance of retrievals. In order to facilitate comparative analysis, the data used in this study are resampled to 25-km spatial resolution. Table 1 summarizes the data used in this study with more details provided in Appendix A-1.

2.2. In-situ data

In-situ SM data are collected from 11 SM observation networks from the International Soil Moisture Network (ISMN) and the Long-Term Agroecosystem Research (LTAR) network to verify the retrieval results of the MTMA algorithm. More details for these in-situ SM observation networks are provided in Appendix A-1.

3. Method

3.1. General description of the algorithm

The zero-order radiative transfer model ($\tau-\omega$ model) (Mo et al., 1982) (Appendix A-2) is generally used to describe the surface

microwave radiative transfer process, and the unknown parameters in $\tau-\omega$ model (see Appendix A-2) mainly include E_p^s (related to soil moisture and roughness), VOD_p and ω_p^{eff}.

Since the observed microwave radiation of land surfaces are the composition of vegetation and soil emissions, the major challenge for accurate retrieval of SM is to decouple the soil and vegetation contributions, which is also the main difference between existing retrieval algorithms. One of the approaches for decoupling soil-vegetation effects is the use of MVIs (Shi et al., 2008; Shi et al., 2019), which minimizes the soil contribution and can be used for deriving vegetation contributions independently without any additional inputs regarding to soil parameters. This MVIs approach has been demonstrated by a previous study (Cui et al., 2015) but only using the H-pol TB with a priory information of ω_p^{eff} based on land cover types. In this study, we further introduce the multi-temporal information to retrieve both VOD_p and ω_p^{eff}, which are expected to be a more accurate estimation of vegetation effects. The retrieved VOD_p and ω_p^{eff} are then used for retrieving soil emissivity (related to SM and soil roughness).

The implementation of the multi-temporal and multi-angular approach in this study is as follows: (1) for each DGG (Discrete Global Grid) node, the SMOS multi-angular TB are processed using the two-step regression method (Zhao et al., 2015b) to reduce TB uncertainties resulted from the RFI and aliasing issues; (2) for each DGG node, the H-pol TB at three angle pairs ((30°, 40°), (35°, 45°) and (40°, 50°)) or the V-pol TB at three angle pairs ((15°, 30°), (20°, 35°) and (25°, 40°)) from two temporal adjacent overpasses are applied to simultaneously retrieve VOD_p and ω_p^{eff} using the MVIs approach, and the soil information (such as the soil emissivity related to soil moisture and roughness) is removed in this process; (3) after correcting the vegetation effects with the retrieved vegetation parameters (VOD_p and ω_p^{eff}), the SM_p and Z_p^s were retrieved simultaneously using the parametric H_p model (Zhao et al., 2015a), which is applied to compute the soil surface emissivity. The flow chart of the MTMA method is shown in Fig. 1.

3.2. Retrieval of vegetation parameters (VOD_p and ω_p^{eff})

Through numerical simulations using the Advanced Integral Equation Model (AIEM), a linear relationship between the soil emissivity at two incidence angles was found (Shi et al., 2019):

$$E_p^s(\theta_2) = \alpha_p\left(\theta_1,\ \theta_2\right) + \beta_p\left(\theta_1,\ \theta_2\right)\cdot E_p^s(\theta_1) \tag{1}$$

where subscript "p" indicates the polarization (H: horizontal, or V: vertical); α_p and β_p are regression coefficients; θ_1 and θ_2 are two incidence angles, for example, θ_1 is 30° and θ_2 is 40°.

Combining the $\tau-\omega$ model with Eq. (1), the linear relationship between the TB at two incidence angles is obtained and the soil information (such as E_p^s) is removed as below:

$$TB_p(\theta_2) = \alpha_p(\theta_1,\theta_2)\bullet V_p^a(\theta_2) + V_p^e(\theta_2) - \beta_p(\theta_1,\theta_2)\bullet\frac{V_p^a(\theta_2)}{V_p^a(\theta_1)} \bullet V_p^e(\theta_1) + \beta_p(\theta_1,\theta_2)\bullet\frac{V_p^a(\theta_2)}{V_p^a(\theta_1)}\bullet TB_p(\theta_1) \tag{2}$$

where V_p^e and V_p^a are vegetation emission term and attenuation term respectively, and written as

$$V_p^e(\theta) = \left(1-\Gamma_p(\theta)\right)\bullet\left(1-\omega_p\right)\bullet\left(1+\Gamma_p(\theta)\right)\bullet T^c \tag{3}$$

$$V_p^a(\theta) = \Gamma_p(\theta)\bullet T^s - \left(1-\Gamma_p(\theta)\right)\bullet\left(1-\omega_p\right)\bullet\Gamma_p(\theta)\bullet T^c \tag{4}$$

where T^c (K) and T^s (K) are the canopy and soil temperature respectively, and are assumed to be equal and expressed by the effective soil temperature (T^{eff}); Γ_p is the vegetation transmissivity ($\Gamma_p = exp\ (-\tau_p^c/\ cos\ (\theta))$); τ_p^c means the VOD_p; ω_p^{eff} is the vegetation effective scattering albedo. The unknowns in Eqs. (2)–(4) include two vegetation parameters (VOD_p and ω_p^{eff}) and coefficients ($\alpha_p(\theta_1,\theta_2)$ and $\beta_p(\theta_1,\theta_2)$). In this study, the SMOS H-pol TBs in three angle pairs (i.e., (30°, 40°), (35°, 45°) and (40°, 50°)) or SMOS V-pol TBs in three angle pairs (i.e., (15°, 30°), (20°, 35°) and (25°, 40°)) are used for retrievals of VOD_p and ω_p^{eff}. The coefficients of $\alpha_p(\theta_1,\theta_2)$ and $\beta_p(\theta_1,\theta_2)$ in H- or V-polarization (Table 2) are obtained by constructing the relationship (i.e., Eq. (1)) using the simulated dataset by the AIEM, and the R is the correlation coefficient between the soil emissivity at two incidence angles. The ranges of SM, surface roughness, incidence angle and other parameters used in the AIEM simulation are shown in Appendix A-3. Therefore, there are only two unknowns of vegetation parameters in Eqs. (2)–(4): VOD_p and ω_p^{eff}.

Table 2
Parameters α and β for different pairs of TBs in incidence angles at H-pol and V-pol obtained by regression of the simulated datasets using AIEM model.

H-pol				V-pol			
θ_1, θ_2	α_H	β_H	R	θ_1, θ_2	α_V	β_V	R
30°, 40°	−0.0467	1.0135	0.9987	15°, 30°	0.0660	0.9501	0.9986
35°, 45°	−0.0557	1.0122	0.9982	20°, 35°	0.0842	0.9363	0.9977
40°, 50°	−0.0652	1.0081	0.9973	25°, 40°	0.1046	0.9207	0.9962

In this study, the multi-temporal approach is further introduced to include more information to enable the simultaneous retrieval of VOD_p and ω_p^{eff} using H-pol or V-pol MVIs. The multi-temporal approach assumes that the vegetation attributes are almost unchanged over a short period, that is, they are set as constants (at several temporal adjacent overpasses), so that the multi-temporal data can be fused together for retrieving a single VOD_p and ω_p^{eff} (Konings et al., 2016, 2017). The multi-temporal approach fuses additional observation to increase the degree of information of input data (Konings et al., 2016, 2017). The increase of the degree of information of input TB data could make the retrieval procedure easier to be convergent and more robust.

In this study, VOD_p and ω_p^{eff} are only assumed to be constant for the two temporal adjacent overpassing time. The multi-temporal data can be applied to the forward model (Eqs. (2)–(4)) and VOD_p and ω_p^{eff} will be resolved simultaneously when the cost function (Eq. (5)) is minimized using the least square method,

$$\underset{X=VOD_p,\omega_p^{eff}}{min} COST_p^{vegetation}(X) = \sum_{t=1}^{N}\sum_{i=1}^{K}\left[TB_p{}^t(\theta_i) - TB_p^{ot}(\theta_i)\right]^2 \Big/ \sigma\left(TB_p^o\right)^2 \tag{5}$$

where t is the overpassing time (as day in this study) of the SMOS satellite, σ is the standard deviation of the SMOS observed TB, N is the number of total satellite overpassing time (days) in consideration, K is the number of observation angle pairs, $TB_p(\theta)$ is simulated TB, $TB_p^o(\theta)$ is SMOS observed TB, X (VOD_p and ω_p^{eff}) is the parameter to be retrieved.

In this study, only the single H-pol or V-pol SMOS TB is used to avoid the assumption that vegetation effects are polarization independent. For each retrieval process, the SMOS multi-angular TB data at three angle pairs ((30°, 40°), (35°, 45°) and (40°, 50°)) for H-pol or three angle pairs ((15°, 30°), (20°, 35°) and (25°, 40°)) for V-pol of N overpasses are obtained, including 3 • N angle pairs observations for either H-pol or V-pol. The multi-temporal data including 3 • N angle pairs observations for H-pol or V-pol will be used to retrieve VOD_p and ω_p^{eff}. N can be taken as a certain value as long as it satisfies the assumption that the change in vegetation attributes is neglectable over a short period and its value is set to 2 days in this study. For a given day t, VOD_p and ω_p^{eff} are retrieved for days (t − 1, t) and for days (t, t + 1). Thus, when two VOD_p and two ω_p^{eff} are obtained, the average values are used as the result of the day following previous studies (Konings et al., 2016; 2017).

The linear relationship (Eq. (2)) between the H-pol (V-pol) TB at two incidence angles was derived by combining $\tau-\omega$ model with a linear

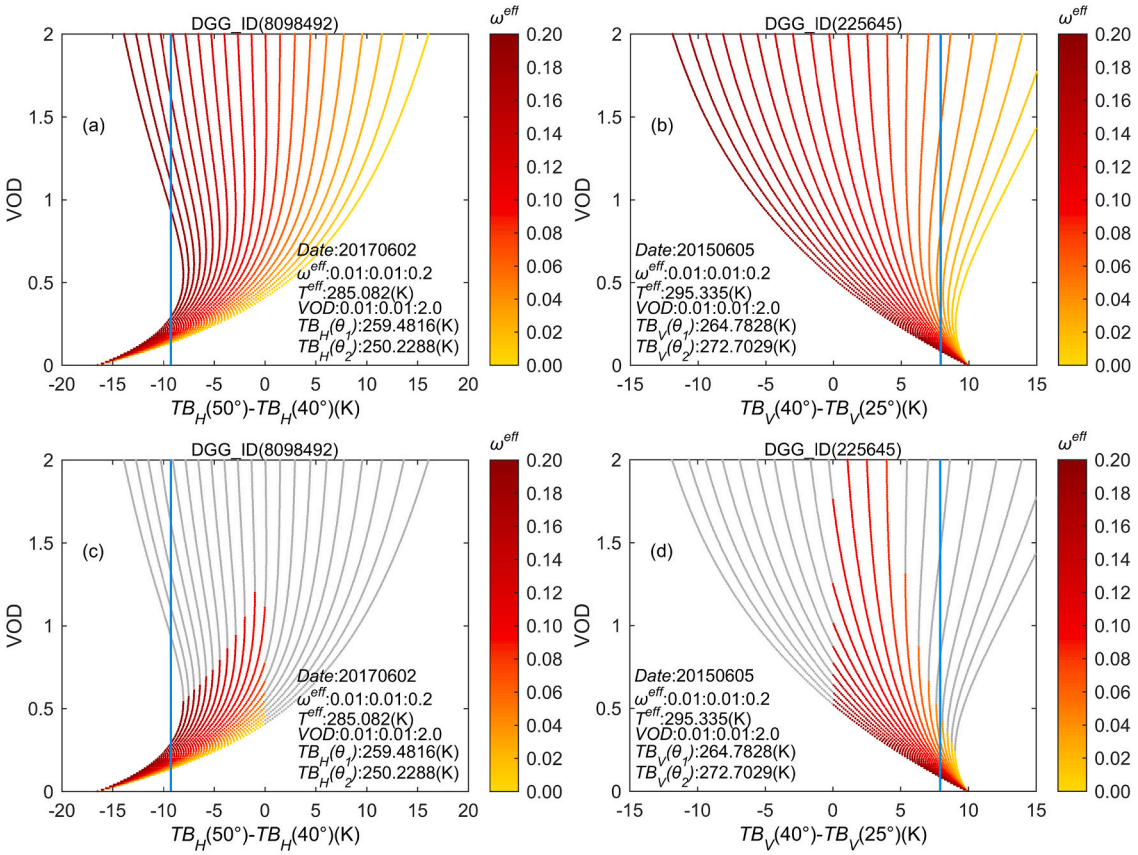

Fig. 2. Simulation results of sensitivity of linear relationship between two incidence angles TB to VOD_p and ω_p^{eff}: (a) H-pol simulation results without constraints; (b) V-pol simulation results without constraints; (c) H-pol simulation results with constraints; (d) V-pol simulation results with constraints. The gray line represents simulations were filtered out according to constraints.

relationship between soil emissivity at two incidence angles (Eq. (1)), however, non physical solutions might be obtained when using Eq. (2) to retrieve the VOD_p and ω_p^{eff}. This is illustrated in Fig. 2 by taking two DGG nodes (DGG ID 8098492, open shrublands; DGG ID 225645, grasslands) as an example. In Fig. 2, the abscissa represents the difference between the $TB_p(\theta_2)_{simulation}$ calculated using Eq. (2) and the SMOS observed $TB_p(\theta_1)$, and the ordinate represents VOD. Besides, the blue line represents the difference between the observed $TB_p(\theta_2)$ and the observed $TB_p(\theta_1)$, and each curve indicates the change of TB difference with VOD at given ω_p^{eff} values. There are two abnormal phenomena in Fig. 2(a) and Fig. 2(b): (1) based on the characteristic of the TB varying with incident angle, that is, the V-pol TB generally increases with the increase of the angle (below Brewster angle), and the H-pol TB decreases with the increase of the angle, however, there are abnormal phenomena: $TB_V(\theta_2)_{simulation} - TB_V(\theta_1) < 0$ (V-pol) or $TB_H(\theta_2)_{simulation} - TB_H(\theta_1) > 0$ (H-pol); (2) the angle characteristics of H-pol or V-pol TB may be weakened with the VOD increases, which means that the TB difference of two incidence angles decreases with the increases of VOD (corresponding to denser vegetation), but there is abnormal phenomenon that the TB difference increases with the increases of VOD.

The above two anomalies may increase the uncertainty of VOD_p and ω_p^{eff} retrievals. Therefore, the constraints needed to be added in the retrieval procedure of VOD_p and ω_p^{eff} using MVIs:

$$\mathrm{TB_V}(\theta_2)_{\mathrm{simulation}} - \mathrm{TB_V}(\theta_1)\rangle 0 \tag{6}$$

$$\mathrm{TB_H}(\theta_2)_{\mathrm{simulation}} - \mathrm{TB_H}(\theta_1)\langle 0 \tag{7}$$

$$\partial\left(\mathrm{TB_V}(\theta_2)_{\mathrm{simulation}} - \mathrm{TB_V}(\theta_1)\right)/\partial\tau < 0 \tag{8}$$

$$\partial\left(\mathrm{TB_H}(\theta_2)_{\mathrm{simulation}} - \mathrm{TB_H}(\theta_1)\right)/\partial\tau > 0 \tag{9}$$

Eq. (6) and Eq. (7) correspond to the above mentioned abnormal phenomena (1), Eq. (8) and Eq. (9) correspond to the above mentioned abnormal phenomenon (2). After adding constraints (Fig. 2(c) and Fig. 2 (d)), the cases with non-physical situation can be filtered out, leading to more physical significance for retrievals of VOD_p and ω_p^{eff}.

3.3. Retrieval of soil parameters (SM_p and Z_p^s)

After retrieving the vegetation parameters, the rough soil emissivity at the 5 • N = 10 for H-pol or 6 • N = 12 for V-pol channels could be simulated, with the SM_p and Z_p^s remaining to be unknowns. These soil parameters (SM_p and Z_p^s) can be retrieved using a parametric soil emissivity model (Eq. (10)) developed by Zhao et al. (2015a):

$$\mathrm{E_p^s}(\theta) = \left(1 - \mathrm{r_p^s}(\theta)\right) \bullet \left[\mathrm{A_p} \bullet exp\left(\mathrm{B_p} \bullet \mathrm{Z_p^{s\,2}} + \mathrm{C_p} \bullet \mathrm{Z_p^s}\right)\right] \tag{10}$$

$$\mathrm{H_p} = \mathrm{A_p} \bullet exp\left(\mathrm{B_p} \bullet \mathrm{Z_p^{s\,2}} + \mathrm{C_p} \bullet \mathrm{Z_p^s}\right) \tag{11}$$

$$A_p = 0.068502 \bullet \theta^2 - 0.058486 \bullet \theta + 0.976321 \tag{12}$$

$$B_p = -0.051377 \bullet \theta^2 + 0.014978 \bullet \theta + 0.045456 \tag{13}$$

$$C_p = 0.601618 \bullet \theta^2 - 0.151848 \bullet \theta - 0.607679 \tag{14}$$

where Z_p^s (cm) is the soil roughness slope parameter and is a function of surface soil root mean square height (S_D) and correlation length (L_c) ($Z_p^s = {S_D}^2/L_c$); r_p^s is the plane reflectivity computed by the Fresnel

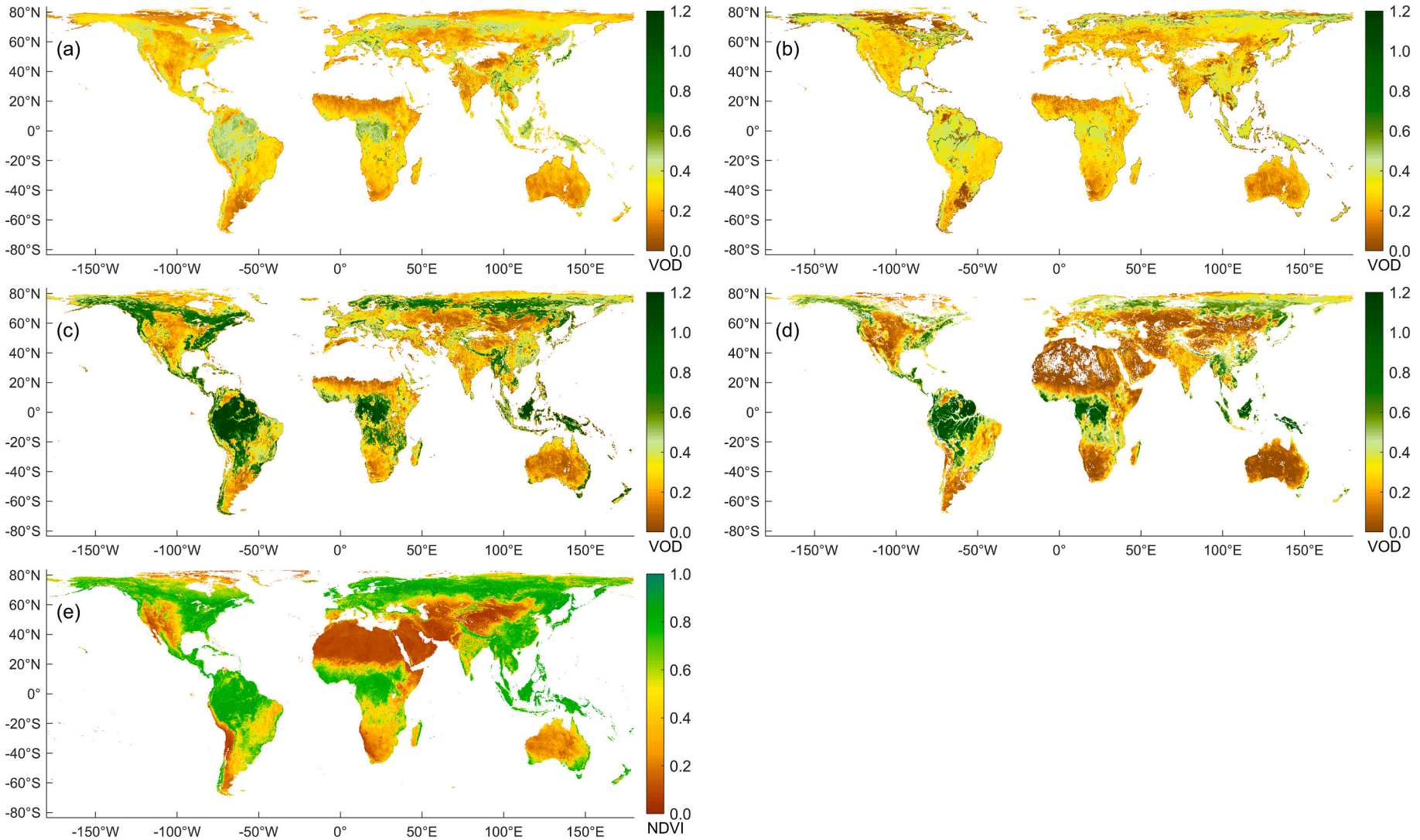

Fig. 3. Global distribution of the monthly-averaged VOD in June 2017: (a) *MTMA-VOD$_H$*, (b) *MTMA-VOD$_V$*, (c) SMOS-L3 VOD at nadir, (d) SMOS-IC VOD, and (e) NDVI (MODIS).

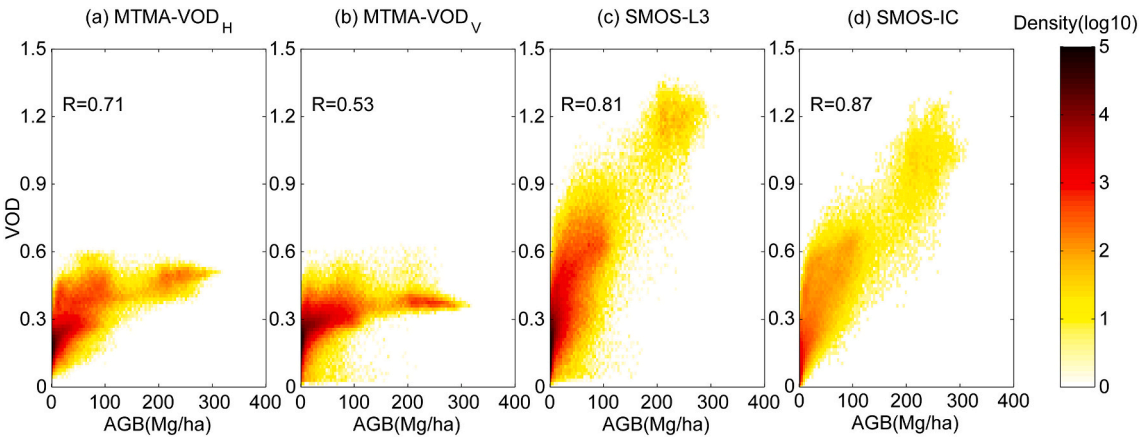

Fig. 4. Density plot of the relationship between AGB and annual average of VOD in 2017

equations; A_p, B_p and C_p are regression coefficients. In this model, the roughness effects H_p is expressed as a function of a roughness slope (Z_p^s) parameter and θ. This parametric H_p model could well describe the complex roughness effects which are depending on both polarization and incidence angle, which is more suitable for SMOS multi-angular observation data.

When auxiliary data (surface effective temperature, soil texture) are obtained, SM_p and Z_p^s can be retrieved using the rough soil emissivity combined with the Mironov dielectric constant model (Mironov et al., 2009) and Fresnel formula, through the cost function as below:

$$\min_{X=SM_p,Z_p^s} \mathrm{COST}_p^{soil}(X) = \sum_{t=1}^{N} \sum_{i=1}^{K} \left[E_p{}^t(\theta_i) - E_p^{ot}(\theta_i) \right]^2 \quad (15)$$

where $E_p{}^t(\theta)$ is the simulated soil emissivity at the overpassing time t, $E_p^{ot}(\theta)$ is soil emissivity calculated from observed TB of SMOS with retrieved vegetation parameters at the overpassing time t, K is the number of observation angle pairs. X (SM_p and Z_p^s) are soil parameters to be retrieved.

In summary, the method proposed in this study combining H-pol or V-pol MVIs with the multi-temporal approach can be used to retrieve global vegetation parameters and soil parameters.

4. Results

The MTMA method proposed in this study was applied to systematically retrieve four parameters (VOD_p, ω_p^{eff}, SM_p and Z_p^s) using the either H-pol or V-pol SMOS multi-angular TB data. Retrievals of these vegetation and soil parameters were evaluated against ground measurements and compared with the other two SMOS products (SMOS-L3 and SMOS-IC).

4.1. Vegetation optical depth retrievals (VOD_p)

Fig. 3 presents the global time-averaged VOD in June 2017 retrieved from the MTMA (*MTMA-VOD$_H$* for H-pol and *MTMA-VOD$_V$* for V-pol) and its global comparison with SMOS-L3 SM, SMOS-IC SM and MODIS NDVI. The four VOD products show comparable patterns at the global scale, with high VOD values over tropical forests located in Central Africa and Amazon areas, and low VOD values in Southern Africa, Australia, and the surrounding areas of Sahara. Except for *MTMA-VOD$_V$*, the VOD values from *MTMA-VOD$_H$*, SMOS-L3 and SMOS-IC in tropical rainforest are higher than that in coniferous forest in northern Asia and Europe. The global distribution of these four VOD products is generally consistent with the corresponding NDVI values and reflects the vegetation characteristics of different land cover types. However, these four VOD products have missing values in different regions, the reason may be that: 1) The missing values in VOD products of MTMA and SMOS-L3 are mainly due to the flagging of non-vegetation areas (such as urban areas, snow and ice, water bodies, wetlands and barren soil) according to the land cover types, or invalid retrievals out of its physical range. 2) The missing values of SMOS-IC VOD products may be due to the quality control using TB_RMSE when model simulated TB differed largely from the measured SMOS TB as affected by RFI or other issues.

In the Eastern Europe, Southeast Asia and tropical forests of Amazon and Congo, the values of *MTMA-VOD$_V$* are lower than those of *MTMA-VOD$_H$*, and in the Northern edge of Russia and Eastern North America, the values of *MTMA-VOD$_H$* are lower than those of *MTMA-VOD$_V$*. The preliminary exploration of the difference between H-pol and V-pol VOD indicate that the vegetation effects can be polarization dependent even at large scales for satellite observations. Konings et al. (2021) also found that the polarization dependence of VOD should be considered in the SM retrieval algorithm due to the large variations of vegetation water content (VOD is related to vegetation water content) within different vegetation components and types, otherwise it might cause the uncertainty and insufficient understanding of VOD retrievals. The difference between *MTMA-VOD$_H$* and *MTMA-VOD$_V$* shown in this study provides a clue to improve the performance of VOD applications in biomass and vegetation water content estimation.

In Europe, the *MTMA-VOD$_H$* and *MTMA-VOD$_V$* are generally high and consistent with high NDVI (meaning abundant vegetation), but the VOD values from SMOS-L3 and SMOS-IC products are relatively lower. In the South Asian Subcontinent, the VOD products derived from all three methods show low values while the NDVI has high values. The RFI in some parts of Europe and South Asia may pollute the SMOS observation TB, resulting in large uncertainties in the VOD retrievals. The Zhao's method (Zhao et al., 2015b) can reduce the influence of RFI and make the refined SMOS TB closer to the theoretical expectations, which is beneficial for both VOD and SM retrievals (also see Section 5.1).

The density plots between AGB data and the annual average VOD in 2017 from *MTMA-VOD$_H$*, *MTMA-VOD$_V$*, SMOS-L3 and SMOS-IC products are shown in Fig. 4. The correlation coefficient R between the VOD retrieved by the MTMA and AGB are 0.71 (*MTMA-VOD$_H$*) and 0.52 (*MTMA-VOD$_V$*) respectively, and are lower than that of SMOS-L3 (0.81) and SMOS-IC (0.87) products. It can be found that *MTMA-VOD$_H$* and *MTMA-VOD$_V$* values over dense vegetated areas are relatively lower than those of SMOS-L3 and SMOS-IC products. Although some studies have been carried out at the local scale, for example, the VOD values in the forest obtained by Ferrazzoli et al. (2002) based on L-band radiometer was close to 0.9, and the VOD values in the low biomass coniferous forest of Les Landes (biomass ~100 t /ha) was close to 0.6–0.7 (Grant et al., 2008), it was difficult to identify which method was closer to the reality, as the validation of VOD at the scale of satellite footprints was currently challenging (Li et al., 2021a). It should be noted that the

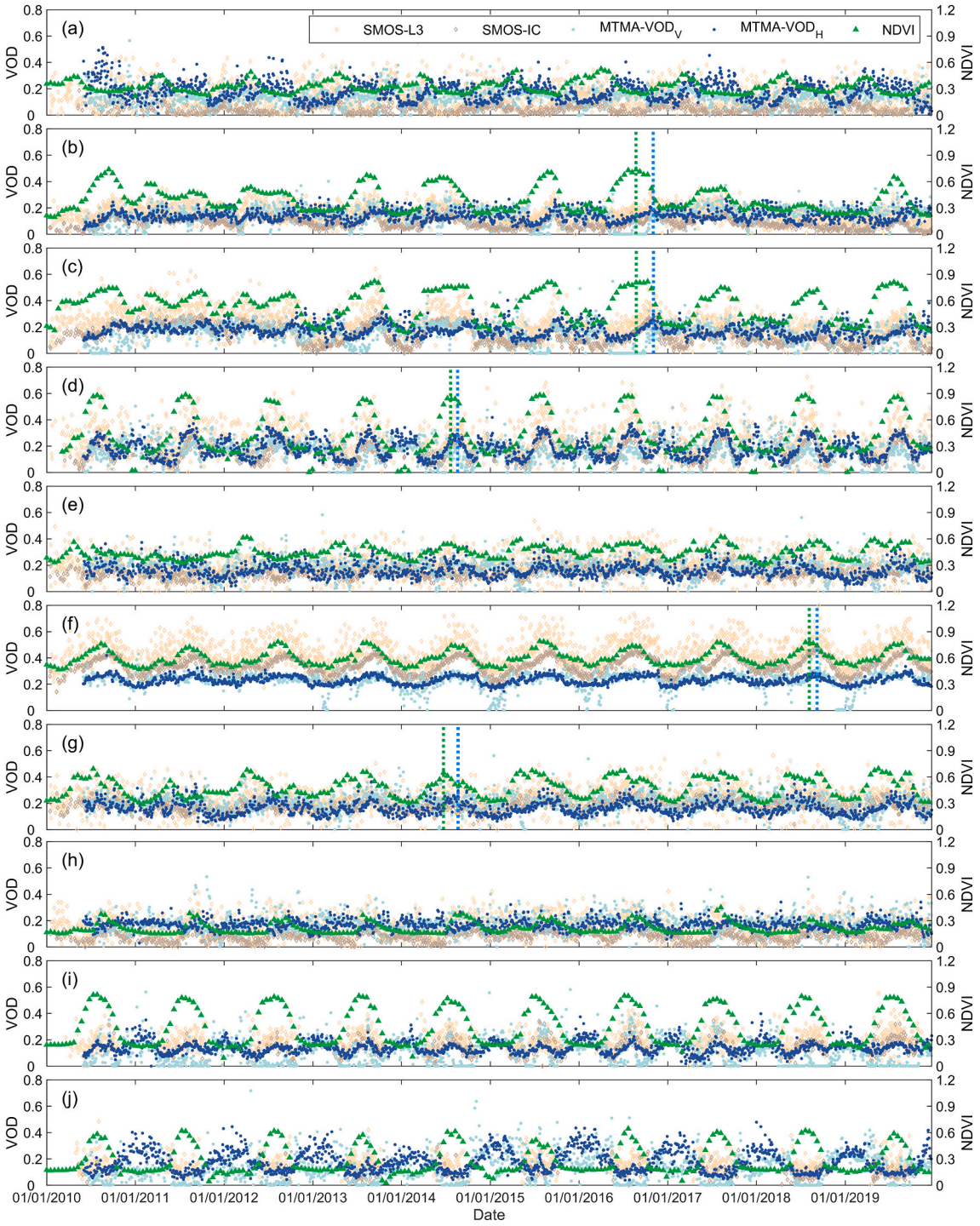

Fig. 5. Time series of VOD from *MTMA-VOD$_H$*, *MTMA-VOD$_V$*, SMOS-L3, and SMOS-IC in 2010–2019 at validation sites: (a) REMEDHUS, (b) Yanco, (c) Kyeamba, (d) South Fork, (e) Fort Cobb, (f) Little River, (g) Little Washita, (h) Walnut Gulch, (i) Maqu, and (j) Naqu. For demonstration, the green dotted line represents the peak value of NDVI and the blue dotted line represents the peak value of VOD. (For interpretation of the references to colour in this figure legend, the reader is referred to the web version of this article)

MTMA-VOD$_H$ and *MTMA-VOD$_V$* might contain larger uncertainties in dense vegetation area, since the difference in TB between different incidence angles was small due to strong vegetation effects (Cui et al., 2015).

The daily VOD at the selected validation sites from January 1, 2010 to December 31, 2019 are shown in Fig. 5. It can be found that the temporal variations of VOD and NDVI at some sites (such as in South Fork and Little River sites) are consistent and the retrieved VOD can reflect the vegetation seasonal fluctuations. However, there is a time lag phenomenon at some sites (such as in Yanco, Kyeamba, South Fork, Little River, and Little Washita) so that the peak value of VOD lags behind NDVI as found by Lawrence et al. (2014) in the crop areas of the USA. The reason of time lag phenomenon may be that the VOD and NDVI reflect different vegetation attributes. The VOD tends to reflect the characteristics of vegetation water content (including leaves, stem, branches and fruits, etc), while the NDVI tends to reflect chlorophyll

Table 3
Numbers of effective VOD retrievals from *MTMA-VOD$_H$*, *MTMA-VOD$_V$*, SMOS-L3 and SMOS-IC in 2010–2019.

	MTMA-VOD$_H$	*MTMA-VOD$_V$*	SMOS-IC	SMOS-L3
REMEDHUS	1640	1634	1063	1852
Yanco	1614	1613	1357	1910
Kyeamba	1572	1571	1290	1829
South Fork	1634	1629	1076	1584
Fort Cobb	1527	1525	1227	1819
Little River	1532	1532	1273	1850
Little Washita	1545	1544	1224	1834
Walnut Gulch	1432	1425	1165	1577
Maqu	1530	1526	427	1075
Naqu	1446	1432	264	741

level of vegetation canopy, specifically the 'greenness' of the canopy. The spectral information obtained from optical sensors might become saturated with crop growth in the optical bands (Tian et al., 2018). However, microwave signals can penetrate through vegetation, and the VOD derived from microwave sensors can still obtain vegetation contribution when the optical band is saturated. The microwave-derived VOD may saturate at a higher vegetation water content and contain more information of the total vegetation water content contributed by leaves, stem, branches and fruits (Jackson et al., 2004; Lawrence et al., 2014).

Differences between the four VOD products can be found in some sites, for example, the VOD values of SMOS-IC are lower than that of *MTMA-VOD$_H$*, *MTMA-VOD$_V$* and SMOS-L3 in REMEDHUS, Kyeamba, Yanco and Walnut Gulch sites, while in the Little River site, the *MTMA-VOD$_H$* and *MTMA-VOD$_V$* values are lower than that of the SMOS-IC and SMOS-L3 products. One of the reasons for the differences between the four VOD products may be the different values of ω_p^{eff} used/retrieved in the different algorithms (Li et al., 2021a).

In Fig. 5, the abnormal fluctuations or daily variation of the *MTMA-VOD$_V$* is larger than that of the *MTMA-VOD$_H$* at some sites (such as in REMEDHUS, South Fork, Walnut Gulch, and Little Washita). The reason may be that when the linear relationship between two incidence angles TB is constructed using the simulation data from the AIEM, the correlation between TB of H-pol in two incidence angles is higher than that of V-pol TB. In other words, the multi-angular information contained in the H-pol observations is more abundant than that of the V-pol observations. Although the algorithm of SMOS-IC is improved with optimized parameters of both ω_p^{eff} and soil roughness, the total number of effective retrievals of SMOS-IC is lower compared to that of SMOS-L3, *MTMA-VOD$_H$*, and *MTMA-VOD$_V$* according to the statistical results in Table 3. It is likely that this is due to the filtering of RFI effects which is conservative in the SMOS-IC product. SMOS-IC VOD values are rather low and have a very small variation at REMEDHUS site. For the snapshot-based retrievals (SMOS-L3 and SMOS-IC), results are more easily affected by noise (such as TB uncertainties, surface heterogeneity and RFI). Non-physical-meaning values (beyond the physical range of parameters) may be obtained in order to force the simulated TB closer to the TB observations, resulting in a reduction in the number of effective retrievals (within a reasonable range, for example, the VOD and SM should not be negative) (Konings et al., 2016, 2017). However, except for Naqu and Maqu sites, the number of effective retrievals of SMOS-L3 VOD generally exceeds the number of effective VOD retrievals from SMOS-IC and MTMA products, mainly because the retrievals affected by RFI are retained in the SMOS-L3 product of 'RE07' version. In Table 3, it can also be seen that the effective VOD number of MTMA products is significantly higher than that of SMOS-IC. The reason could be: (1) the VOD_p and ω_p^{eff} are retrieved using microwave vegetation indices (Eq. (2)) in which the soil information is eliminated and enables the decoupling of soil and vegetation signals in the retrieval process; (2) SMOS L1C TB data are refined by the two-step regression method (Zhao et al., 2015b) and become closer to theoretical expectation, which means that more

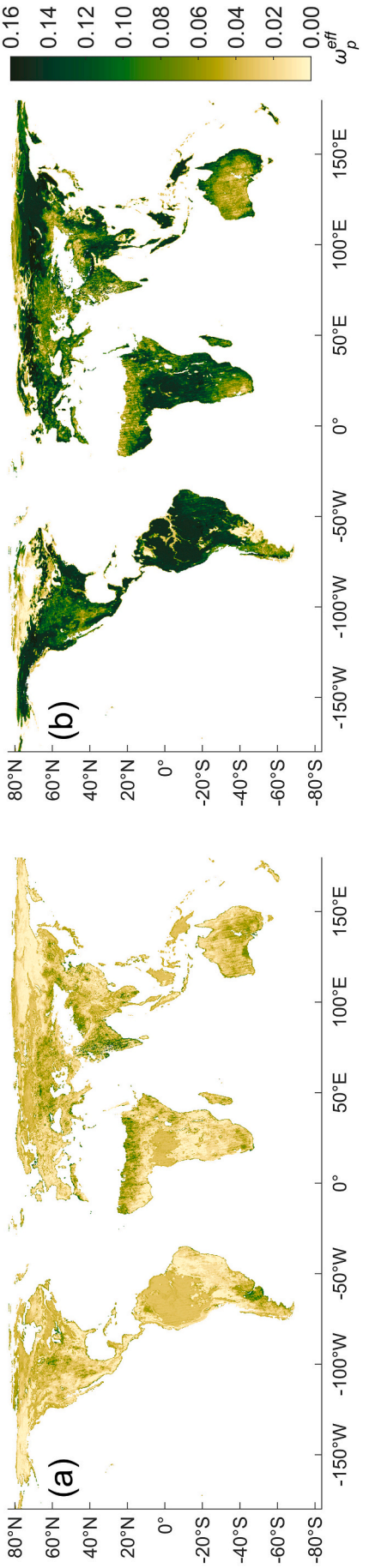

Fig. 6. Retrievals of ω_p^{eff} based on SMOS multi-angular TB data in June 2017: (a) *MTMA-ω_H^{eff}* and (b) *MTMA-ω_V^{eff}*.

Table 4
Effective scattering albedo obtained by different methods

landcover	SMAP-SCA	SMOS-IC	SMAP-DCA	*MTMA-*ω_H^{eff}	*MTMA-*ω_V^{eff}
water bodies	0.000	0.000	0.000	0.000	0.000
evergreen needleleaf forest	0.050	0.060	0.070	0.041	0.104
evergreen broadleaf forest	0.050	0.060	0.070	0.035	0.126
deciduous needleleaf forest	0.050	0.060	0.070	0.035	0.141
deciduous broadleaf forest	0.050	0.060	0.070	0.043	0.115
mixed forests	0.050	0.060	0.070	0.037	0.138
closed shrublands	0.050	0.100	0.080	0.031	0.076
open shrublands	0.050	0.080	0.070	0.032	0.069
woody savannas	0.050	0.060	0.080	0.020	0.122
savannas	0.080	0.100	0.100	0.021	0.109
grasslands	0.050	0.100	0.070	0.035	0.087
permanent wetlands	0.000	0.100	0.100	0.000	0.000
croplands-average	0.050	0.120	0.060	0.046	0.106
urban and built-up kands	0.030	0.100	0.080	0.000	0.000
cropland/natural vegetation mosaics	0.065	0.120	0.100	0.034	0.077
snow and ice	0.000	0.100	0.080	0.000	0.000
barren	0.000	0.120	0.050	0.000	0.000

locations with TB data affected by RFI may also be used for the retrieval after refinement; (3) even if the required TB data are missing or lead to a failed retrieval, the multi-temporal approach can make up for the deficiency by introducing temporal adjacent overpassing data.

4.2. Effective scattering albedo retrievals (ω_p^{eff})

The global monthly average results of ω_p^{eff} in June 2017 are shown in the Fig. 6. The values of *MTMA-*ω_H^{eff} for H-pol and *MTMA-*ω_V^{eff} for V-pol in the tropical forest areas of the Amazon basin in South America and of the Congo basin in Africa are higher than those in the low vegetation areas, and this result is similar to the distribution of ω_p^{eff} retrieved by Konings et al. (2016, 2017). The mean values of *MTMA-*ω_p^{eff} for different vegetation types are also calculated and compared with several reference data of ω_p^{eff} as shown in Table 4. The values of *MTMA-*ω_H^{eff} and *MTMA-*ω_V^{eff} for low vegetation (grass and savannas) are in the range of 0–0.046 and 0–0.122 respectively, and the values for high vegetation (forest) are 0.035–0.043 and 0.104–0.138, respectively. The values of *MTMA-*ω_V^{eff} for different vegetation types are significantly higher than those of *MTMA-*ω_H^{eff}. The scattering effects of the vegetation layer depends on the vegetation structure (stalks, branches, trunks and leaves) and vegetation water content, etc. The scattering contribution of different vegetation components depends on their leaves/stems orientation, size and shape, etc. Kurum (2013) found that for vegetation with stem-dominated scattering (such as corn), the dependence of vegetation scattering for V-pol was stronger than that of H-pol due to the stalks near vertical orientation. Zhao et al. (2020a) also found that the scattering in H-pol in vegetation layer was less than that in V-pol and increases with increasing incidence angle. Although the dependence of ω_p^{eff} on polarization were mainly found at ground-based observations or model simulations, it was found that the scattering effects of vegetation is still different at pixel scales of satellite observations. Furthermore, Konings et al. (2016) found that the ω_p^{eff} in SM retrieval algorithms had more significant influence on the SM retrievals than VOD. Therefore, to improve the quality of SM and VOD retrievals, the polarization dependence of vegetation effects in terms of both attenuation (VOD) and scattering (ω^{eff}) is considered in the proposed MTMA algorithm.

4.3. Soil moisture retrievals (SM_p)

Using the MTMA approach proposed in this study, the global monthly average SM results (*MTMA-*SM_H for H-pol and *MTMA-*SM_V for V-pol) in June 2017 are obtained and compared with the SMOS-L3 and SMOS-IC products, as shown in Fig. 7. The spatial distribution of all the four products is generally consistent and reflects the spatial variations of SM in different climatic regions. The SMOS-IC products have the higher value compared with SMOS-L3 and *MTMA-*SM_H and *MTMA-*SM_V in predominantly wet soil areas, such as the Amazon Forest of South America, India and so on. In the densely vegetated area, the sensitivity of the SMOS radiometer to SM is reduced due to the strong attenuation of the ground emission signal by vegetation, therefore the SM retrievals are significantly affected by the VOD retrievals in these dense vegetation areas. As mentioned early, the TB difference between two incidence angles is small over densely vegetated surface, which will weaken the linear relationship between TB at two incidence angles, so that the low VOD values lead to relative lower values of SM when compared with SMOS-IC. Moreover, the difference between *MTMA-*SM_H and *MTMA-*SM_V is also calculated. The Fig. 7(e) shows that the values of *MTMA-*SM_H are generally higher than that of *MTMA-*SM_V, and the areas with large difference between these two SM mainly occurred in the tropical forests of Amazon and Congo, the forest area of North of Eurasia, the forest area of Southeast Asia and the forest area of Northwest and Northeast of North America. The reason for these differences in SM may be attributed to the different vegetation effects as shown in Fig. 3. To be noted, it is expected to have very close SM yet different VOD for different polarizations.

Fig. 8 presents the time series of daily SM retrievals from January 1, 2010 to December 31, 2019 using our method against the ground in-situ measurements at sites, and the values from SMOS-L3 and SMOS-IC are also given as references. According to the Fig. 8, Fig. 9 and statistical metrics (Table 5), the *MTMA-*SM_H and *MTMA-*SM_V are in good agreement with the in-situ data with the overall $R > 0.75$, indicating that the *MTMA-*SM_p can capture temporal dynamic changes of SM. In addition, the ubRMSE of *MTMA-*SM_H varies from 0.022 to 0.057 m^3/m^3 and is better than that of *MTMA-*SM_V (0.029 to 0.063 m^3/m^3). In terms of correlation, SMOS-IC obtained the best results over most sites outside China (REMEDHUS, Yanco, Fort Cobb, Little River, Little Washita and Walnut Gulch sites), while results of SMOS-IC and SMOS-L3 are poorer in China as shown in several previous studies (Liu et al., 2019; Li et al., 2020). This can be explained by the strong RFI effects which strongly affect the SMOS products in China. So, in China, comparison of obtained results is difficult, as results strongly depend on the use of RFI filtering and on the use of TB product (SMOS-IC and MTMA did not use the same input TB data). The improved results obtained by the MTMA in China strongly suggest that the use of TB refined by the two-step regression approach to filter the RFI is very performant in regions densely affected by RFI.

In addition, except for the REMEDHUS site, the R of *MTMA-*SM_H is lower than that of *MTMA-*SM_V, but the ubRMSE of *MTMA-*SM_V is generally greater than that for the *MTMA-*SM_H. The different performance between *MTMA-*SM_H and *MTMA-*SM_V products may be due to the uncertainty of the vegetation parameters retrievals (Fig. 5). Although the performance of *MTMA-*SM_V is not as good as that of *MTMA-*SM_H and SMOS-IC products in most sites, it is still comparable with SMOS-L3 product. According to the statistical metrics of combining data from all the sites together, it can be found that the R of *MTMA-*SM_H is 0.775, and are relatively higher than that of *MTMA-*SM_V ($R = 0.756$), SMOS-IC ($R = 0.750$) and SMOS-L3 ($R = 0.733$) products. Moreover, the ubRMSE of *MTMA-*SM_H (0.050 m^3/m^3) and *MTMA-*SM_V (0.054 m^3/m^3) is also lower than that of SMOS-IC (0.058 m^3/m^3) and SMOS-L3 (0.066 m^3/m^3) products. Overall, the *MTMA-*SM_H and *MTMA-*SM_V by the MTMA method performed satisfactorily compared with SMOS-L3 and SMOS-IC products in the 11 validation sites used in this study. The improved performance of the retrievals using MTMA may come from several reasons: (1) The two-step regression method is used to refine the SMOSL1C TB, which reduced the influence of RFI and aliasing on the observed TB. The details of impact assessment of the two-step regression

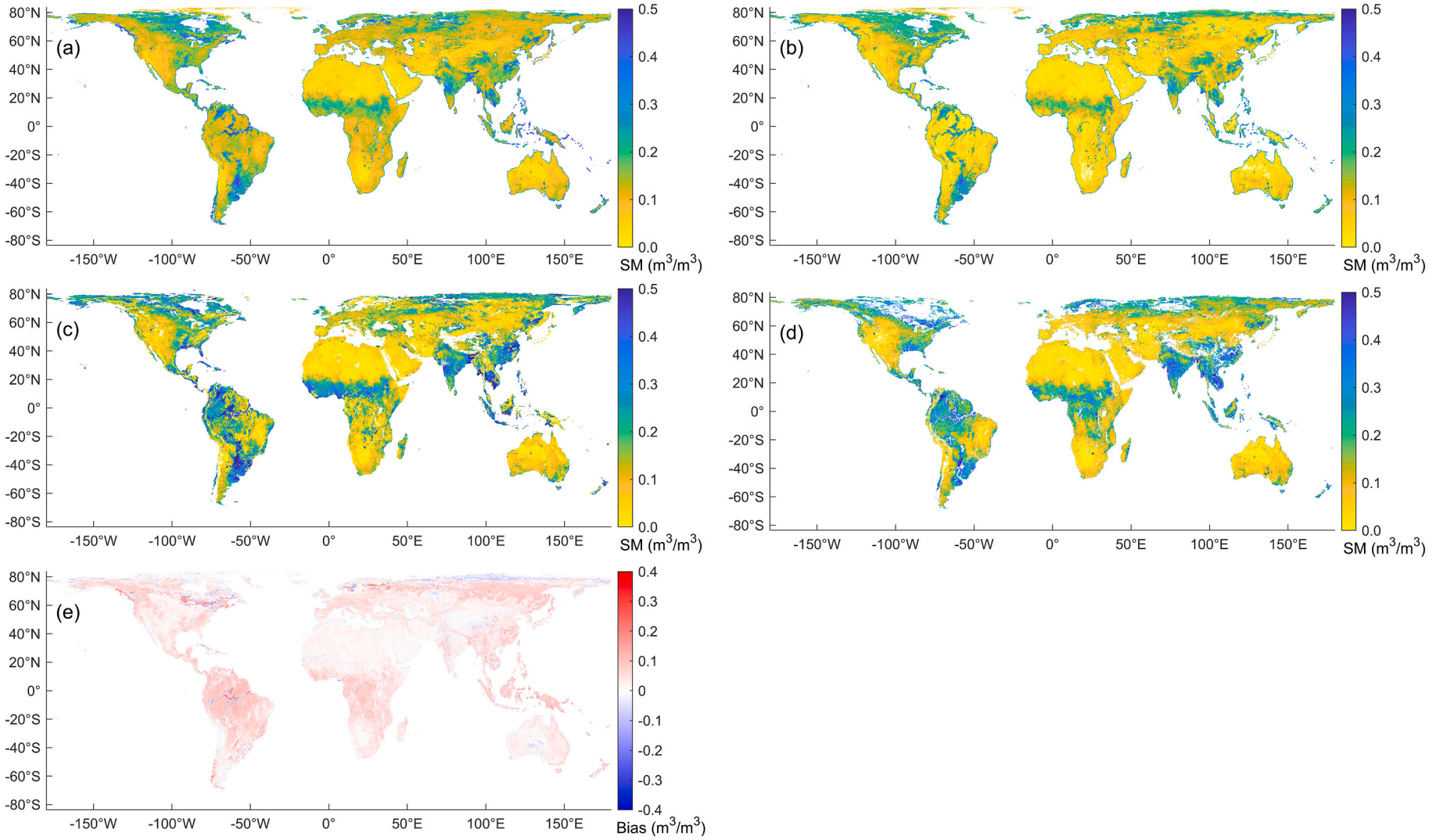

Fig. 7. Global distribution of the time-averaged SM (sm^3/sm^3) in June 2017: (a) *MTMA-SM*$_H$, (b) *MTMA-SM*$_V$, (c) SMOS-L3 SM, (d) SMOS-IC SM and (e) the difference (*MTMA-SM*$_H$ minus *MTMA-SM*$_V$) between *MTMA-SM*$_H$ and *MTMA-SM*$_V$.

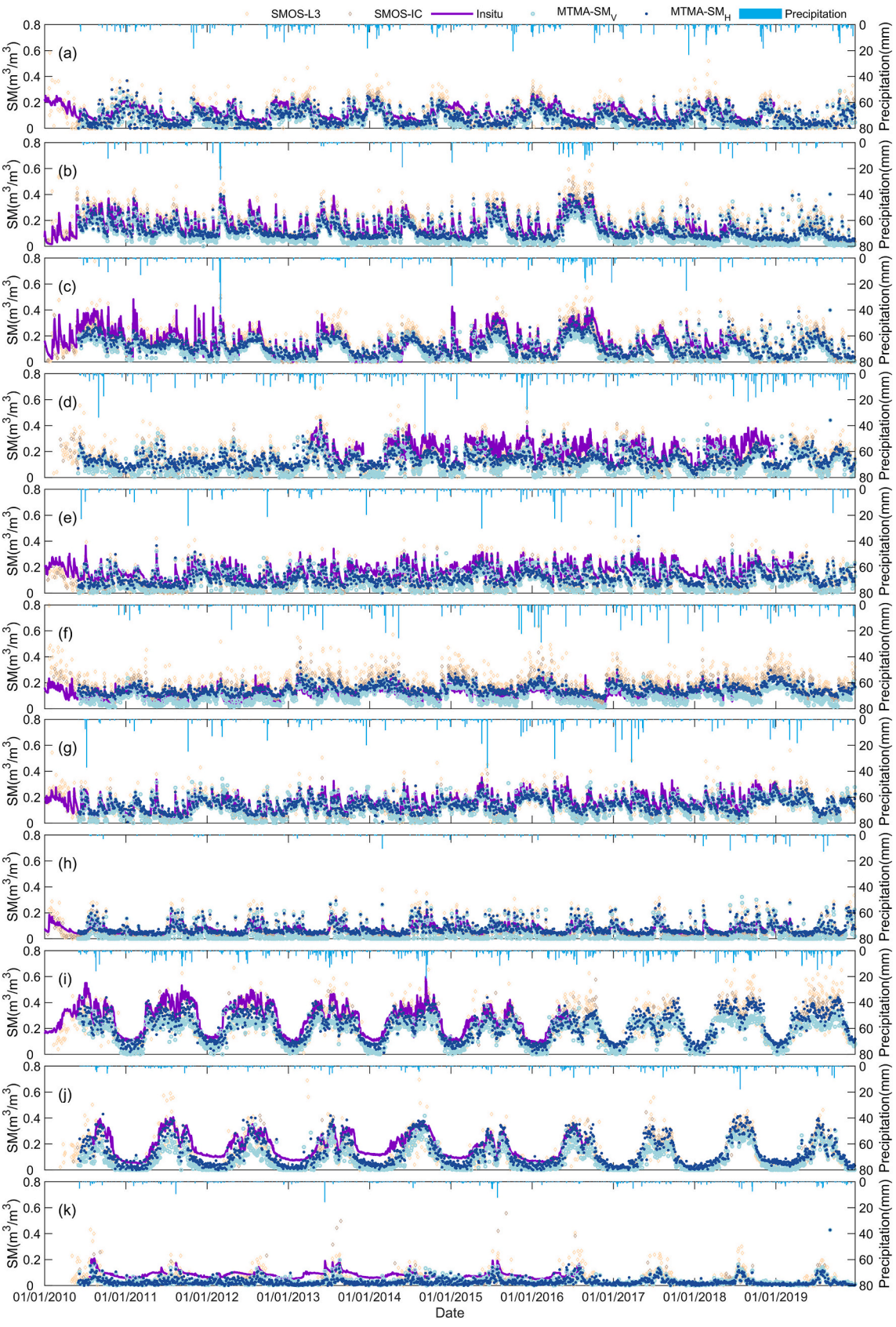

Fig. 8. Time series of SM retrievals in 2010 to 2019 at different sites: (a) REMEDHUS, (b) Yanco, (c) Kyeamba, (d) South Fork, (e) Fort Cobb, (f) Little River, (g) Little Washita, (h) Walnut Gulch, (i) Maqu, (j) Naqu and (k) Ali. Precipitation data are also plotted as reference of wetness fluctuation.

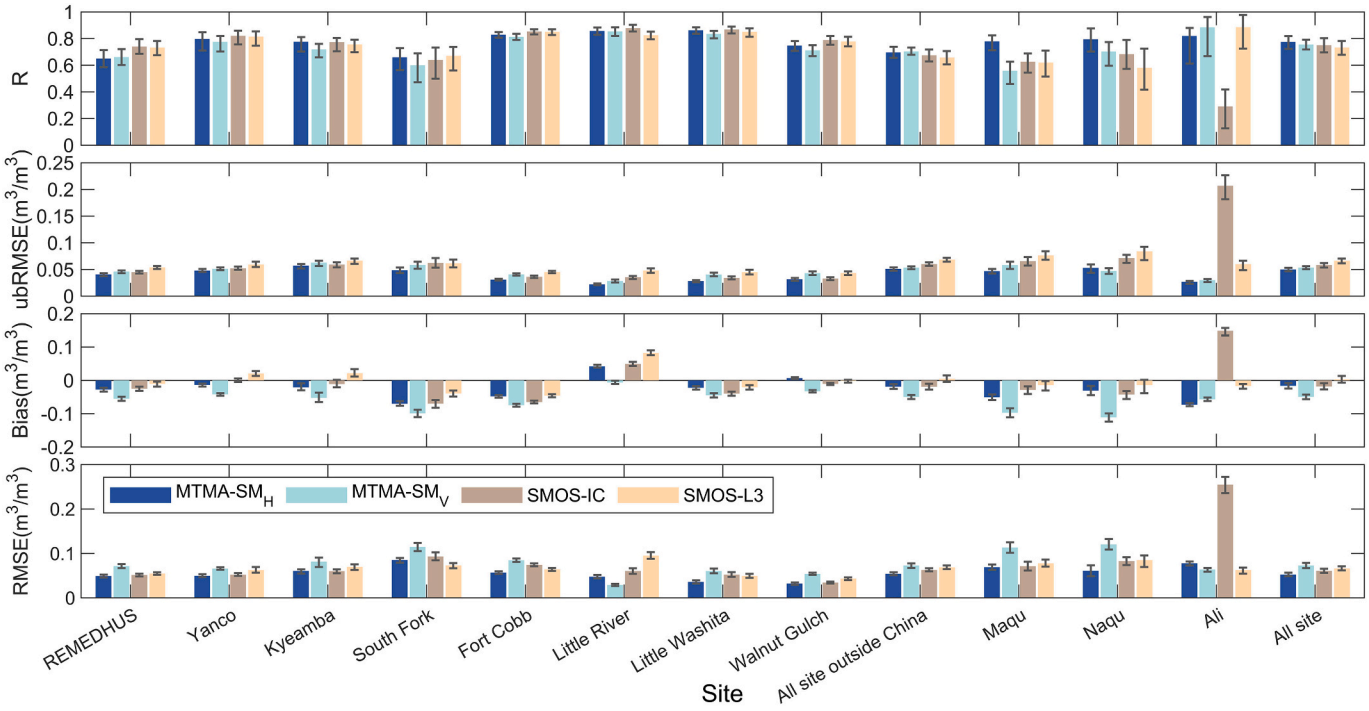

Fig. 9. The performance metrics with 95% confidence intervals for SM retrievals at validation sites

method are discussed in Section 5.1, and it is found that the adoption of the two-step regression method can increase the number of retrievals with improved correlation and reduced uncertainties. (2) The use of MVIs, which can minimize the soil contribution, may lead to a more accurate retrieval of VOD over low to medium vegetated areas (validation sites), thus reduces the uncertainties in decoupling of the vegetation and soil information. (3) The multi-angular and multi-temporal information is used to increase the abundance of information from observations, in support of additionally retrieval of the dynamic ω_p^{eff} and Z_p^s, which reduces the uncertainty in SM retrieval, rather than using empirical/fixed values in the retrieval algorithm. In Section 5.2–5.3, the importance of dynamic retrieval of ω_p^{eff} and Z_p^s parameters is discussed.

4.4. Soil roughness retrievals (Z_p^s)

Soil surface roughness is also an important parameter influencing the L-band microwave emission. The increase of surface roughness leads to the increase of microwave emission, and reduces its sensitivity to SM. In this study, the Z_p^s ranging from 0.04 to 0.22 cm is also retrieved with SM_p and vegetation parameters (VOD_p and ω_p^{eff}), and compared with several existing roughness parameter products/auxiliary data: the surface roughness parameter h (0 to 0.16 cm) used by the single channel algorithm of SMAP products obtained according to the land cover type; the surface roughness h (0 to 0.996 cm) used by the DCA algorithm for SMAP (Chaubell et al., 2020); the surface roughness h (0 to 1 cm) retrieved based on the multi-angular TB of SMOS (Parrens et al., 2016). For comparison, roughness effects of H_p is obtained according to the bare soil emissivity model related to roughness parameter (($H_p = exp\,(-h \bullet cos^{N_p^r}(\theta))$, $N_p^r = -1$) or Eq. (11)), which decreased with the increase in the roughness parameter (Z_p^s or h). The global monthly average value of H_p in June 2017 (Fig. 10) is obtained and compared with the H_p values calculated using the roughness parameter of the existing products/auxiliary data.

In Fig. 10(c), the h values provided by the SMAP single channel algorithm (SCA) are mainly empirical values based on land cover types, and the differences between different vegetation types are relatively small, and therefore the dynamic range of spatial distribution of H_p is small. The H_p retrieved by the MTMA method (Fig. 10(a) and 10(b)) have similar results with SMAP-DCA (Fig. 10(d)) in areas of north of Eurasia, northeastern North American and southern South America with relative strong roughness effects, and in central Australia with weak roughness effects. Moreover, the H_p retrieved by the MTMA (Fig. 10(a) and 10(b)) have similar results with SMOS roughness data (Fig. 10(e)) in areas of most Africa with relatively low roughness effects over forests and high roughness effects in southern Africa. However, in the Sahara Desert of northern Africa, the spatial distribution of the H_p values of Fig. 10(d) and 10(e) are opposite to MTMA-H_H for H-pol and MTMA-H_V for V-pol. Based on the C-band TB data of AMSR-E, Pellarin et al. (2009) found that the roughness in the Sahara and the Sahel have a spatial variability due to the influence of topography (sand dunes), which is similar to the results of MTMA-H_H and MTMA-H_V. The values of H_p in Fig. 10(a), 10(b), 10(d) and 10(e) are also relatively low (corresponding to strong roughness effects) in the dense forests of the Amazon in the South America and the Congo in Africa due to the existence of a litter layer in the dense forest, and the "effective surface roughness" formed by the superposition of the litter layer on the ground surface results in increase in roughness parameter (Saleh et al., 2006; Grant et al., 2007).

In this study, the mean values of H_p parameter of different land cover types for these five roughness data are also statistically calculated. In Table 6, the ranges of H_p parameter values of different land cover types for MTMA-H_H, MTMA-H_V, SMAP-DCA-H_p and SMAP-SCA-H_p are 0.824–0.889, 0.804–0.861, 0.679–0.820, 0.901–0.936 respectively. The value differences between different land cover types for these four roughness data are relatively small, and the range of H_p values is also small. Moreover, for the same vegetation type, the difference of H_p values between the MTMA-H_H or MTMA-H_V and SMAP-DCA-H_p or SMAP-SCA-H_p is also relatively small (about 0.1). However, SMOS-H_p is obviously different for different land cover types. In SMOS algorithm (Parrens et al., 2016), h is retrieved by combining with VOD, so the distribution of H_p parameters may be more related to the distribution of vegetation. Therefore, H_p parameters of different land cover types vary greatly, with lower values in high vegetation types (such as forest) and higher values in low vegetation types (such as grasslands, closed shrublands and open shrublands). In general, the global spatial

Table 5
The validation metrics of *MTMA-SM$_H$*, *MTMA-SM$_V$*, SMOS-L3 and SMOS-IC using in-situ measurements from 2010 to 2019 (Number1 represents the number of retrievals used for calculating metrics, Number2 represents the total number of effective retrievals for each product)

Network/Sites	Product	R	Bias (m^3/m^3)	RMSE (m^3/m^3)	ubRMSE (m^3/m^3)	Number1	Number2
REMEDHUS	*MTMA-SM$_H$*	0.650	−0.028	**0.049**	**0.041**	782	1640
	MTMA-SM$_V$	0.662	−0.055	0.072	0.046		1104
	SMOS-IC	**0.741**	−0.025	0.052	0.045		1221
	SMOS-L3	0.733	**−0.011**	0.055	0.054		1944
Yanco	*MTMA-SM$_H$*	0.797	−0.014	**0.050**	**0.048**	1130	1614
	MTMA-SM$_V$	0.776	−0.042	0.066	0.051		1603
	SMOS-IC	**0.821**	**0.000**	0.052	0.052		1358
	SMOS-L3	0.815	0.021	0.063	0.059		1917
Kyeamba	*MTMA-SM$_H$*	**0.776**	−0.021	0.061	**0.057**	897	1572
	MTMA-SM$_V$	0.719	−0.052	0.082	0.063		1335
	SMOS-IC	0.773	**−0.011**	**0.060**	0.059		1283
	SMOS-L3	0.756	0.021	0.070	0.067		1842
South Fork	*MTMA-SM$_H$*	0.660	−0.070	0.085	**0.049**	589	1634
	MTMA-SM$_V$	0.600	−0.099	0.115	0.058		1507
	SMOS-IC	0.640	**−0.070**	0.093	0.062		1069
	SMOS-L3	**0.671**	−0.039	**0.073**	0.062		1707
Fort Cobb	*MTMA-SM$_H$*	0.829	−0.048	**0.057**	**0.031**	999	1527
	MTMA-SM$_V$	0.814	−0.074	0.085	0.041		1398
	SMOS-IC	**0.853**	−0.065	0.074	0.036		1219
	SMOS-L3	0.851	**−0.046**	0.064	0.045		1835
Little River	*MTMA-SM$_H$*	0.857	0.042	0.048	**0.022**	1077	1532
	MTMA-SM$_V$	0.854	**−0.006**	**0.029**	0.029		1532
	SMOS-IC	**0.879**	0.049	0.061	0.035		1273
	SMOS-L3	0.825	0.082	0.095	0.048		1850
Little Washita	*MTMA-SM$_H$*	0.863	−0.022	**0.036**	**0.028**	1072	1545
	MTMA-SM$_V$	0.835	−0.045	0.060	0.040		1509
	SMOS-IC	**0.868**	−0.040	0.053	0.034		1222
	SMOS-L3	0.851	**−0.021**	0.049	0.045		1837
Walnut Gulch	*MTMA-SM$_H$*	0.748	0.007	**0.032**	**0.032**	1063	1432
	MTMA-SM$_V$	0.712	−0.033	0.054	0.043		1432
	SMOS-IC	**0.788**	−0.011	0.035	0.033		1185
	SMOS-L3	0.778	**−0.002**	0.044	0.043		1686
All sites outside China	*MTMA-SM$_H$*	0.696	−0.019	**0.054**	**0.051**	7609	11,064
	MTMA-SM$_V$	**0.704**	−0.050	0.073	0.053		9988
	SMOS-IC	0.675	−0.019	0.063	0.060		8766
	SMOS-L3	0.658	**0.005**	0.069	0.069		13,247
Maqu	*MTMA-SM$_H$*	**0.779**	−0.051	**0.069**	**0.047**	221	1530
	MTMA-SM$_V$	0.559	−0.097	0.113	0.058		1530
	SMOS-IC	0.627	−0.029	0.072	0.066		437
	SMOS-L3	0.620	**−0.014**	0.078	0.077		1340
Naqu	*MTMA-SM$_H$*	**0.795**	−0.031	**0.061**	0.053	102	1446
	MTMA-SM$_V$	0.703	−0.111	0.120	**0.047**		1446
	SMOS-IC	0.684	−0.043	0.083	0.071		277
	SMOS-L3	0.580	**−0.014**	0.085	0.084		1152
Ali	*MTMA-SM$_H$*	0.820	−0.073	0.078	**0.027**	143	1409
	MTMA-SM$_V$	**0.884**	−0.057	0.064	0.030		1409
	SMOS-IC	0.291	0.149	0.255	0.207		236
	SMOS-L3	0.886	**−0.017**	**0.063**	0.060		604
All Sites	*MTMA-SM$_H$*	**0.775**	−0.017	**0.053**	**0.050**	8035	16,881
	MTMA-SM$_V$	0.756	−0.050	0.073	0.054		15,805
	SMOS-IC	0.750	−0.018	0.061	0.058		10,923
	SMOS-L3	0.733	**0.003**	0.066	0.066		18,155

distribution of H_p parameter of these five roughness data is different. The advantage of our method is that the roughness parameter is directly retrieved together with SM and vegetation parameters. However, it is almost not possible to validate the retrieved roughness at satellite pixel/grid scales, as the surface roughness is a measure of roughness comparable to wavelength of the SMOS sensor (21 cm for L-band). And the roughness retrieval at satellite pixel/grid scale is more like a parameter optimization, and the roughness parameter may become a "conceptual" parameter that suits corresponding algorithms. The goal of this study is to provide a fair comparison of different roughness data, but it is difficult to identify which data is most desireable.

5. Discussions

5.1. Impact assessment of the two-step regression

In this study, the SMOS L1C TB data are re-processed using the two-step regression method (Zhao et al., 2015b) to reduce the uncertainty resulted from the RFI and aliasing issues. To evaluate the influence of the two-step regression method on the SM and VOD retrievals, we compared the retrievals using TB with or without the two-step regression refinement at the validation sites in 2016. We also compared SMOS L3 TB product which is generated without using the two-step regression method.

From retrievals of VOD with the same algorithm of MTMA (Fig. 11), the abnormal fluctuation of VOD by using SMOS L3 TB is more obvious than the VOD retrieved by using the refined TB, although there is a consistency between the two. The reason is that the SMOS L3 TB data may not show a reasonable TB dependence on incidence angles and polarization, that is, V-pol TB generally increases with the incident angle while H-pol TB decreases with the incident angle. The MTMA algorithm proposed in this study is utilizing the TB dependence on incidence angles, the unreasonable variations of SMOS L3 TB with incidence angle will lead to erroneous retrievals. Therefore, the two-step regression

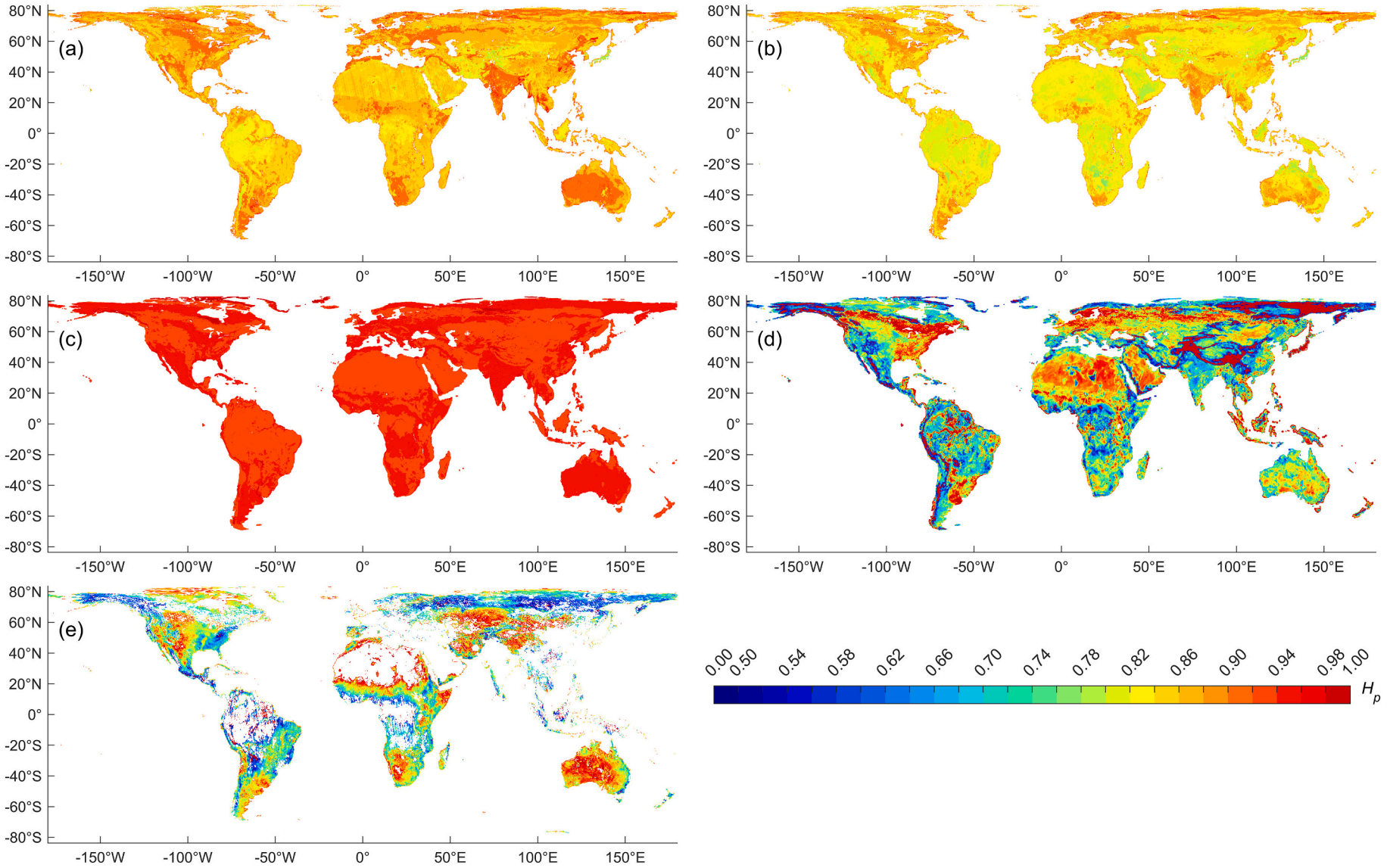

Fig. 10. Global distribution of the time-averaged $H_{p\ in\ June\ 2017}$: (a) the MTMA-H_H obtained using retrievals of Z_H^s by our method with H-pol TB, (b) the MTMA-H_V obtained using retrievals of Z_V^s by our method with V-pol TB, (c) the H_p obtained using soil roughness h of SMAP single channel algorithm (SCA) ancillary data, (d) the H_p obtained using soil roughness h of SMAP dual channel algorithm (DCA) ancillary data and (e) the H_p obtained using soil roughness h estimated by SMOS data.

Table 6
The H_p parameter of different land cover types obtained by different methods

		Static			Dynamic			
ID	landcover	SMAP-DCA	SMAP-SCA	SMOS	MTMA-H_H	MTMA-H_V	Standard deviation(H-pol)	Standard deviation(V-pol)
0	water bodies	–	–	–	–	–	–	–
1	evergreen needleleaf forest	0.800	0.902	0.295	0.839	0.824	0.025	0.027
2	evergreen broadleaf forest	0.733	0.901	0.132	0.824	0.804	0.025	0.026
3	deciduous needleleaf forest	0.694	0.911	0.278	0.829	0.810	0.018	0.019
4	deciduous broadleaf forest	0.752	0.917	0.237	0.831	0.812	0.026	0.028
5	mixed forests	0.819	0.913	0.288	0.836	0.811	0.025	0.028
6	closed shrublands	0.713	0.930	0.757	0.886	0.849	0.022	0.029
7	open shrublands	0.679	0.936	0.664	0.889	0.860	0.023	0.028
8	woody savannas	0.738	0.918	0.295	0.868	0.850	0.022	0.025
9	savannas	0.688	0.925	0.417	0.843	0.816	0.022	0.025
10	grasslands	0.702	0.919	0.586	0.846	0.811	0.024	0.025
11	permanent wetlands	–	–	–	–	–	–	–
12	croplands-average	0.756	0.934	0.359	0.889	0.862	0.026	0.022
13	urban and built-up kands	–	–	–	–	–	–	–
14	cropland/natural vegetation mosaics	0.756	0.930	0.361	0.863	0.841	0.030	0.025
15	snow and ice	–	–	–	–	–	–	–
16	barren	0.708	0.905	0.563	0.826	0.812	0.038	0.028

method used for refining SMOS L1C TB data is an essential step for the implementation of the MTMA.

According to Fig. 12 and Table 7, the SM retrievals using the refined TB performs much better compared with that using the original SMOS L3 TB data at most of the sites in terms of R or ubRMSE, except at REMEDHUS and Walnut Gulch sites where the R of $TB_{Refined}$-SM_V are smaller than that of TB_{SMOSL3}-SM_V. Moreover, the total amount of SM retrievals by the refined TB is significantly more than that retrieved by the original SMOS L3 TB. Comparison was not carried out at the three validation sites (Ali, Maqu and Naqu sites) in China due to too few days (<15 days) with successful SM retrievals using the original SMOS L3 TB, possibly resulted by small amount of available original SMOS L3 TB data in 2016 due to the influence of RFI. Therefore, we believe that it is necessary to reprocess SMOS L1C TB with the two-step regression method to reduce the influence of the RFI.

5.2. Importance of additional retrieval of ω_p^{eff}

Davenport et al. (2005) and Fernandez-Moran et al. (2017b) confirmed that errors in ω_p^{eff} may increase the uncertainties in the SM and VOD retrievals. The ω_p^{eff} is dependent on polarization and varies over time, which should not be ignored in SM retrieval algorithm. However, most algorithms utilize constant (calibrated) values dependent on land cover types to reduce the number of unknows. In this study, the ω_p^{eff}, as one of the important factors affecting the SM retrievals, is simutaneously retrieved together with VOD_p using the proposed MTMA method. To demonstrate the significance of dynamic retrieval of ω_p^{eff}, we selected the data from 2015 to 2016 to retrieve SM using either dynamic retrievals of ω_p^{eff} or setting ω_p^{eff} as constants, respectively, and compared the accuracy of the SM retrievals at validation sites. The constant values of ω_p^{eff} are obtained from different satellite products, as listed in Table 4.

The comparison of metrics between SM retrievals using dynamic ω_p^{eff} values and fixed ω_p^{eff} values is shown in Fig. 13. The abscissa represents the metrics of SM retrieved by dynamic ω_p^{eff} values, and the ordinate represents the metrics of SM retrieved by fixed ω_p^{eff} values obtained from SMOS-IC, SMAP-SCA and SMAP-DCA products, respectively. The first row in Fig. 13 shows that there is almost no difference between the R of H-pol SM retrieved by dynamic ω_H^{eff} values and static ω_H^{eff} values, but the ubRMSE of SM retrieved by dynamic ω_H^{eff} values is slightly lower. The second row in Fig. 13 shows that the R values of V-pol SM retrieved by static ω_V^{eff} values from the SMOS-IC product are slightly higher than that of SM retrieved using dynamic ω_V^{eff} values, and there are also cases where the R values of SM retrieved using the static ω_V^{eff} values from SMAP-SCA and SMAP-DCA products are lower than that using the dynamic ω_V^{eff} values. Furthermore, the ubRMSE of V-pol SM retrieved by static ω_V^{eff} values from SMOS-IC are moderately lower than that based on dynamic ω_V^{eff} values at Fort Cobb, Little River and Walnut Gulch sites, but the ubRMSE values of SM retrieved by dynamic ω_V^{eff} values are smaller than that based on static ω_V^{eff} at Yanco, South Fork and Maqu sites. Meanwhile, the ubRMSE values of V-pol SM retrieved by using dynamic ω_V^{eff} values and using the static ω_V^{eff} values provided by SMAP-SCA and SMAP-DCA products are comparable.

In summary, compared with setting the ω_p^{eff} as constants in SM retrieval, the performance of SM obtained using dynamic ω_p^{eff} values is more satisfactory in particular for the H-pol SM in terms of ubRMSE. Considering that the ω_p^{eff} should vary with locations and time, due to the high heterogeneity of vegetation and its seasonality, dynamic pixel-wise ω_p^{eff} is expected to lead to more robustness in both SM and VOD retrievals (Konings et al., 2016). Moreover, our results reveals that the ω_p^{eff} is polarization dependent at satellite pixel/grid scales, as shown in Fig. 6. These results provid an opportunity to further understand the spatio-temporal variation of vegetation scattering at a global scale, which is worthy of fruther exploration.

5.3. Dependence of roughness effects on soil moisture

In this study, the daily roughness parameter Z_p^s was simultaneously retrieved together with SM. According to Eq. (11), the parameter H_p describing roughness effects was obtained. Since it is almost not possible to validate the roughness parameter at satellite pixel/grid scales, we analyzed the dependence of roughness effects on soil moisture to prove its validity. Previous studies have indicated that the roughness effects may vary with soil moisture content due to the smoothing effect of precipitation and a 'dielectric roughness' layer under the visible soil layer (Wigneron et al., 2001; Schneeberger et al., 2004; Escorihuela et al., 2007). Peng et al. (2017) found that the H_p was a power exponential function of SM_p:

$$H_p = m_p \bullet SM_p^{n_p} \tag{16}$$

where m_p and n_p are fitted coefficients. The data from 2015 to 2016 at validation sites are used to explore the dependence of roughness on soil moisture at satellite scale.

By fitting Eq. (16) with the MTMA retrieved SM and roughness, it is found there is a dependence of roughness on soil moisture at five sites (Yanco, Little River, Maqu, Naqu and Ali sites) with R^2 >0.35 for both of H-pol and V-pol, while various site-dependent constant roughness values are observed at other sites. Therefore, we selected these five sites for analysis. The scatter plots of H_p and SM_p (under conditions below field capacity) using the data from all the five sites are shown in Fig. 14, with fitted parameters including m_p, n_p and R^2 shown in Table 8. The

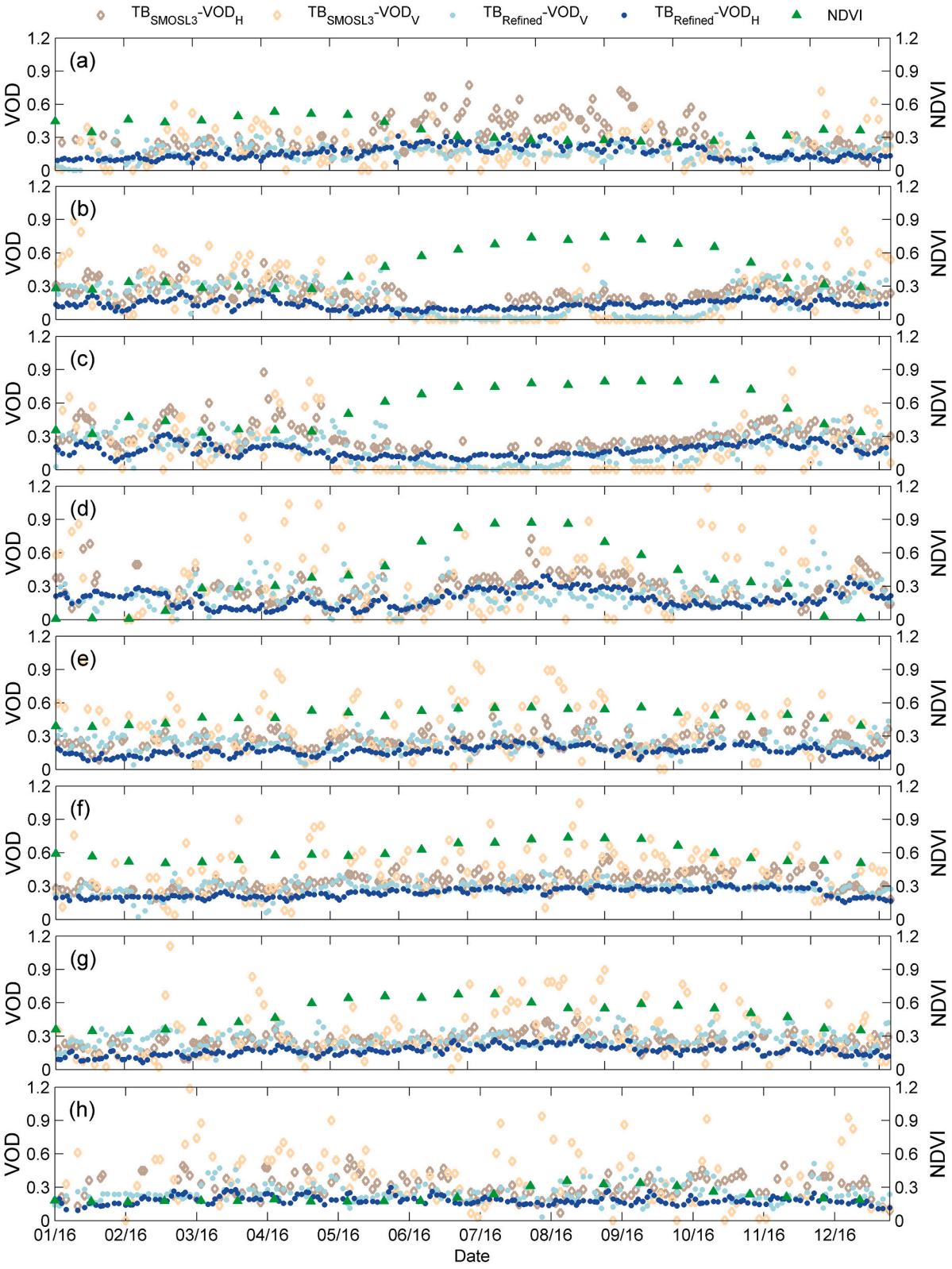

Fig. 11. Time series of VOD retrieved by MTMA using refined H-pol TB ($TB_{Refined}$-VOD_H), refined V-pol TB ($TB_{Refined}$-VOD_V), unrefined H-pol TB (TB_{SMOSL3}-VOD_H) and unrefined V-pol TB (TB_{SMOSL3}-VOD_V) in 2016 at sites: (a) REMEDHUS, (b) Yanco, (c) Kyeamba, (d) South Fork, (e) Fort Cobb, (f) Little River, (g) Little Washita, and (h) Walnut Gulch.

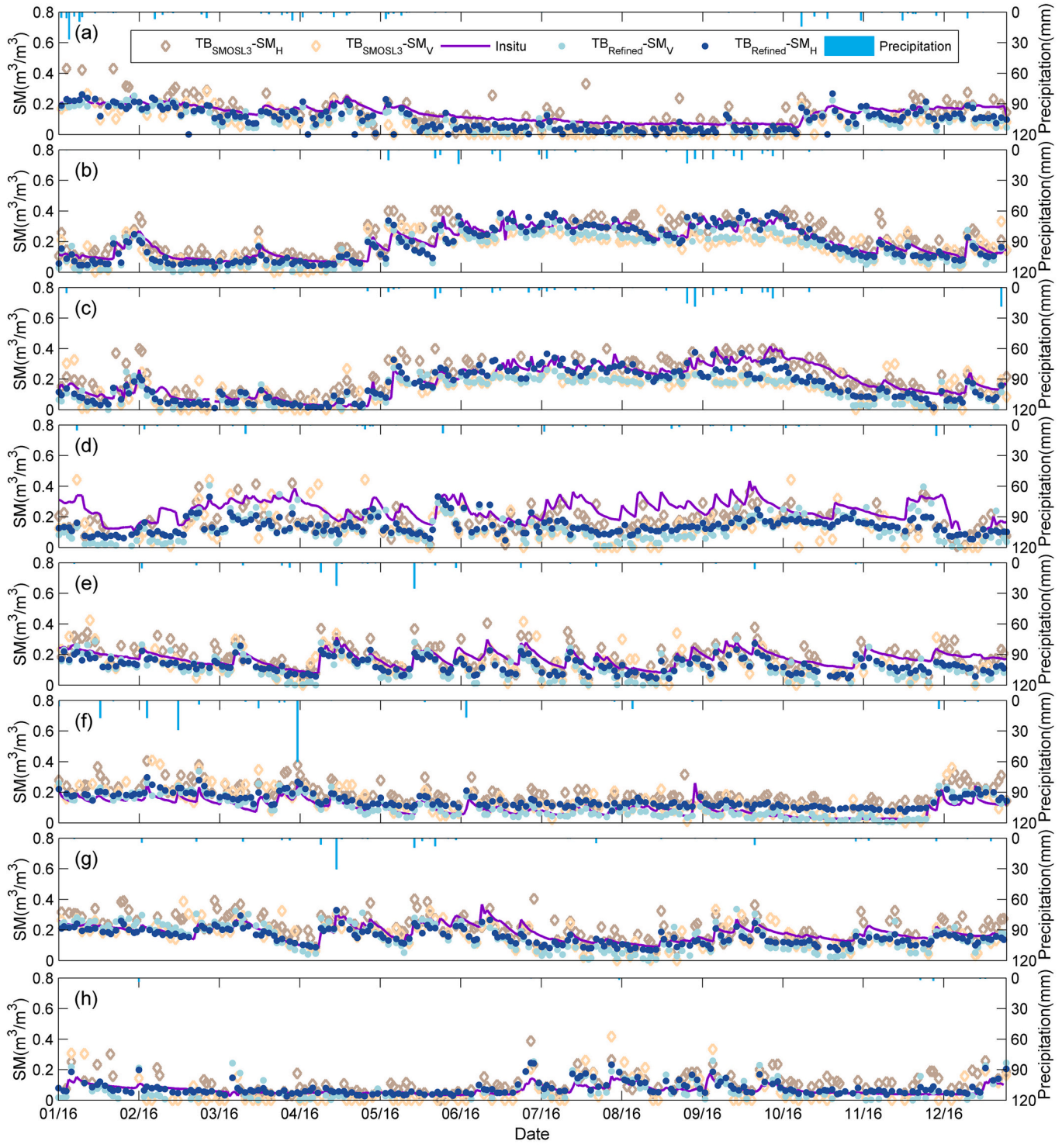

Fig. 12. Time series of SM retrieved by the MTMA using refined H-pol TB ($TB_{Refined}$-SM_H), refined V-pol TB ($TB_{Refined}$-SM_V), unrefined H-pol TB (TB_{SMOSL3}-SM_H) and unrefined V-pol TB (TB_{SMOSL3}-SM_V) in 2016 at sites: (a) REMEDHUS, (b) Yanco, (c) Kyeamba, (d) South Fork, (e) Fort Cobb, (f) Little River, (g) Little Washita, and (h) Walnut Gulch.

plot shows that the R^2 between H_p and SM_p exceeds 0.6 and the H_p increases as SM increases, indicating a decrease in roughness effects. It is reasonable that the high soil moisture (after precipitation) may smooth the soil surface (i.e., low roughness effects), while the low soil moisture may cause an additional 'dielectric roughness' layer (i.e., high roughness effects) due to increased penetration depth. It is shown that the dependence of H_p on SM is different for different polarization. Moreover, with the increase of SM, the sensitivity of H_p to SM_p decreases. Our results indicate that the dependence of roughness effects on soil moisture still exists at satellite pixel/grid scales and can be explained by an exponential function for those sites where the retrieved roughness parameter changes over time.

5.4. Limitations and quality control

Although the MTMA achieved a promising results in retrieving SM,

Table 7
The quantitative validation results of $TB_{Refined}$-SM_H, $TB_{Refined}$-SM_V, TB_{SMOSL3}-SM_H and TB_{SMOSL3}-SM_V using in-situ measurements in 2016

Network/Sites	Product	R	Bias (m^3/m^3)	RMSE (m^3/m^3)	ubRMSE (m^3/m^3)	Number of retrievals
REMEDHUS	$TB_{Refined}$-SM_H	**0.801**	−0.042	**0.058**	**0.040**	**209**
	TB_{SMOSL3}-SM_H	0.713	**−0.005**	0.068	0.067	146
	$TB_{Refined}$-SM_V	0.785	**−0.052**	**0.065**	**0.040**	**158**
	TB_{SMOSL3}-SM_V	**0.792**	−0.064	0.079	0.045	110
Yanco	$TB_{Refined}$-SM_H	**0.916**	**−0.012**	**0.045**	**0.043**	**208**
	TB_{SMOSL3}-SM_H	0.840	0.032	0.065	0.056	160
	$TB_{Refined}$-SM_V	**0.860**	−0.045	**0.066**	**0.048**	**203**
	TB_{SMOSL3}-SM_V	0.728	**−0.033**	0.077	0.069	133
Kyeamba	$TB_{Refined}$-SM_H	**0.856**	**−0.026**	**0.059**	**0.053**	**204**
	TB_{SMOSL3}-SM_H	0.830	0.031	0.070	0.062	149
	$TB_{Refined}$-SM_V	**0.748**	−0.065	**0.090**	**0.062**	**181**
	TB_{SMOSL3}-SM_V	0.613	**−0.046**	0.095	0.083	119
South Fork	$TB_{Refined}$-SM_H	**0.526**	−0.105	0.119	**0.057**	**219**
	TB_{SMOSL3}-SM_H	0.506	**−0.068**	**0.097**	0.070	141
	$TB_{Refined}$-SM_V	**0.471**	−0.122	**0.143**	**0.076**	**208**
	TB_{SMOSL3}-SM_V	0.401	**−0.109**	0.147	0.099	105
Fort Cobb	$TB_{Refined}$-SM_H	**0.821**	−0.046	**0.055**	**0.029**	**201**
	TB_{SMOSL3}-SM_H	0.722	**0.009**	0.056	0.056	164
	$TB_{Refined}$-SM_V	**0.765**	−0.062	0.079	**0.048**	**195**
	TB_{SMOSL3}-SM_V	0.649	**−0.034**	**0.077**	0.069	114
Little River	$TB_{Refined}$-SM_H	**0.922**	**0.046**	**0.050**	**0.019**	**195**
	TB_{SMOSL3}-SM_H	0.790	0.090	0.098	0.041	169
	$TB_{Refined}$-SM_V	**0.909**	**0.008**	**0.033**	**0.032**	**195**
	TB_{SMOSL3}-SM_V	0.775	0.044	0.072	0.057	122
Little Washita	$TB_{Refined}$-SM_H	**0.838**	**−0.031**	**0.043**	**0.029**	**202**
	TB_{SMOSL3}-SM_H	0.620	0.032	0.070	0.062	169
	$TB_{Refined}$-SM_V	**0.779**	−0.033	**0.063**	**0.054**	**202**
	TB_{SMOSL3}-SM_V	0.634	**−0.022**	0.067	0.063	118
Walnut Gulch	$TB_{Refined}$-SM_H	**0.784**	**0.012**	**0.030**	**0.028**	**187**
	TB_{SMOSL3}-SM_H	0.611	0.045	0.069	0.053	135
	$TB_{Refined}$-SM_V	0.639	**−0.002**	**0.054**	**0.054**	**119**
	TB_{SMOSL3}-SM_V	**0.773**	−0.011	0.072	0.071	91

the MTMA algorithm developed in this study has some limitations as discussed below.

(i) The MTMA algorithm might be less applicable to V-pol TB observations due to the less variability of V-pol TB with incidence angles, and the polarization dependence of VOD at the satellite pixel/grid scale found in this study needs further confirmation. Many previous studies have indicated that the VOD is dependent on frequency, polarization, and incidence angle (Jackson and Schmugge, 1991; Wigneron et al., 2004b; Zhao et al., 2020b; Konings et al., 2021; Zhao et al., 2021), although most algorithms assume that there is no dependence on polarization to reduce the number of unknowns. However, it is important to retrieve VODs at different polarizations, which should be useful to separate the contributions of vegetation water content, biomass, and vegetation structure, etc., to VODs, since the sensitivities of microwave remote sensing to vegetation vary with frequency and polarization (Baur et al., 2019; Konings et al., 2021). Although retrieval of VOD at different polarizations is important, it is almost not possible to validate the value of VOD, especially at the satellite pixel/grid scale. Moreover, the VOD is a conceptual variable from the view of radiative transfer model rather than a physical variable, and the VOD values could be different from different algorithms, such as the difference between our results with that from SMOS-IC, and the difference between SMOS-IB AMSR2 and CCI (Wang et al., 2021). Despite the uncertainties in the VOD results, this study, for the first time, derived and demonstrated the global L-band VODs at different polarizations.

(ii) The MTMA algorithm is more prone to saturation in densely vegetated areas (AGB above 200 Mg/ha) compared to other algorithms (SMOS L3 and SMOS-IC). Different from iterative algorithms based on forward modelling, the MTMA algorithm utilizes analytical solutions between TB observations at different incidence angles to first retrieve the vegetation properties. Our approach is able to separate the soil and vegetation contributions, but it is highly relying on the variability of TB with incidence angles. For dense vegetated areas, the vegetation effects (VOD) are too strong to have significant variation in observed TB, and thus lead to less degree of information to derive an effective value of VOD. In addition, some studies have also found that VOD products (such as SMAP SCA and DCA products) incorporating optical remote sensing information in the algorithms showed obvious saturation (Li et al., 2022). The main reason might be that optical remote sensing data (NDVI) was more sensitive to the features of the upper vegetation layer information and was easier to be saturated than VOD. This saturation phenomenon of our VOD products may limit the interest of using VOD to monitor the phenological dynamics of vegetation over forests.

Previous studies have shown that there was a linear correlation between the L-band VOD and AGB, and the correlation coefficient can exceeded 0.85 (Brandt et al., 2018; Li et al., 2020; Li et al., 2021b). However, in Fig. 4, the VOD values retrieved by MTMA are saturated when the AGB values exceed 200 Mg/ha. To demonstrate the sensitivity of our polarized VOD to AGB, we averaged values of VOD and AGB for different vegetation types (evergreen needleleaf forest (ENF), evergreen broadleaf forest (EBF), deciduous needleleaf forest (DNF), deciduous broadleaf forest (DBF), mixed forest (MF), closed shrublands (CS), open shrublands (OS), woody savannas (WS), savannas (S), grasslands (G), croplands (C), cropland/natural vegetation mosaic (CNVM)) at the global scale in 2017 as shown in Fig. 15. It can be found that the VOD is linear correlated with AGB when AGB values are lower than 100 Mg/ha except for EBF. However, when AGB values exceed 200 Mg/ha for EBF, the values of VOD do not increase anymore, which may indicate that the uncertainty of VOD retrievals using MTMA is relatively large for EBF. The high AGB values can lead to a transmissivity value close to 0, thus significantly weaken the difference between TB from various incidence angles. The MTMA algorithm, which is highly relying on the variability

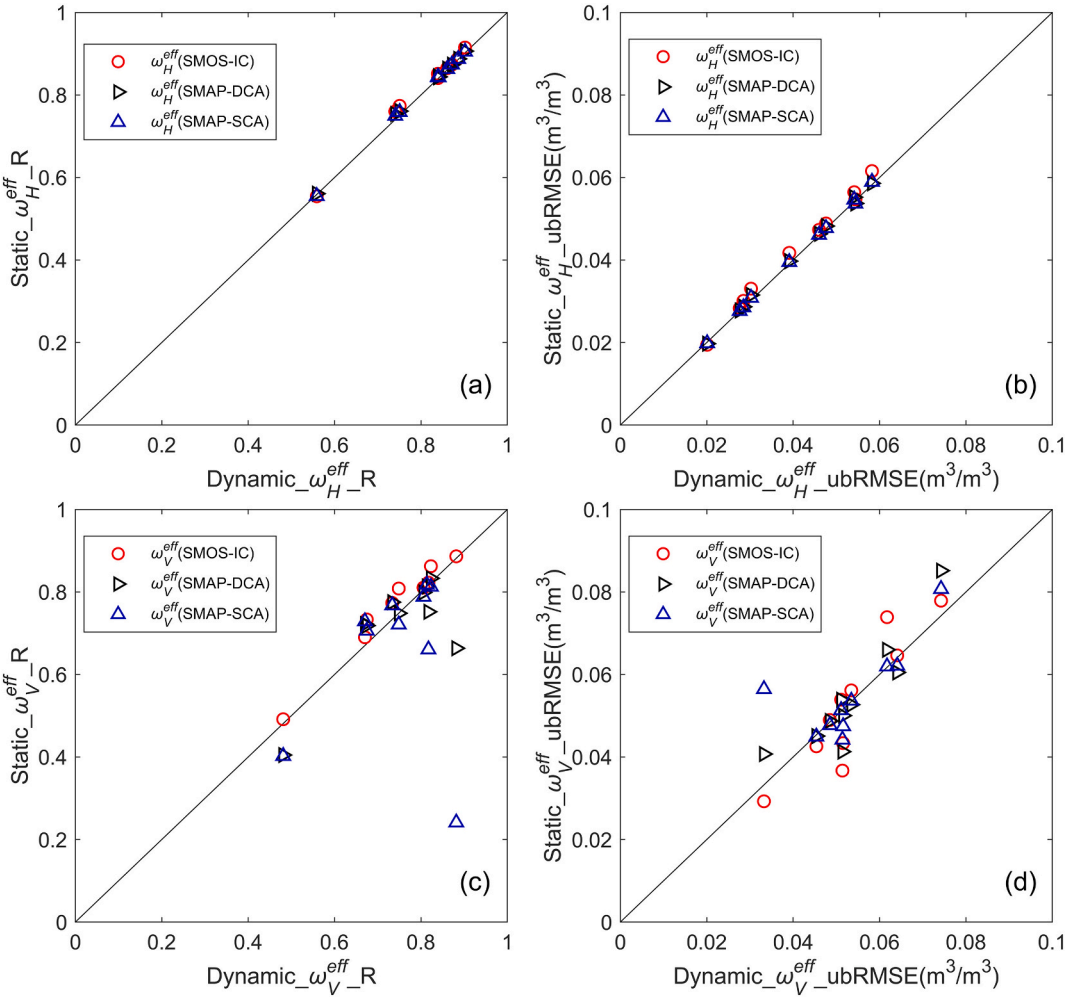

Fig. 13. Dynamic-based ω_p^{eff} metrics versus static-based ω_p^{eff} metrics (R and ubRMSE) at 10 validation sites in 2015–2016.

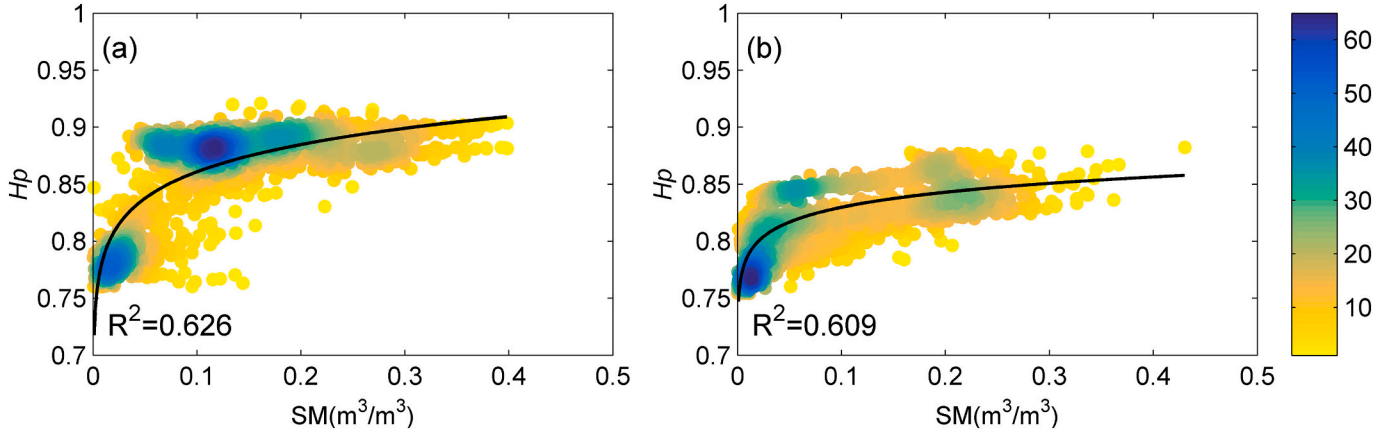

Fig. 14. Estimated roughness effect parameter H_p versus SM at five validation sites (Yanco, Little River, Maqu, Naqu and Ali sites): (a) H-pol and (b) V-pol in 2015–2016.

of TB with incidence angles, would have a greater uncertainty in retrievals due to less degree of information over forested areas. Therefore, we filtered out the SM retrievals with the AGB values exceeding 200 Mg/ha as quality control (Fig. 16). Compared with Fig. 7, it can be found that the areas with large uncertainty of SM retrievals are mainly distributed in the tropical forest areas of Amazon, Congo, Indonesia, and New Guinea.

It is worth noting that the retrieval of VOD_p and ω_p^{eff} in this study is not constrained in cost function as done in SMOS L2/L3 and SMOS-IC algorithms, and the VOD_p retrievals in dense forest area is low and saturated. For example, the range of $MTMA\text{-}\omega_H^{eff}$ in dense forest area is 0.04–0.05, and the range of $MTMA\text{-}VOD_H$ is 0.5–0.6. However, Cui et al. (2015) assumed that the ω_p^{eff} in dense forest area was 0.1, and obtained VOD retrievals of > 1, indicating that the vegetation parameter

Table 8
Fitted parameters m_p, n_p and R^2 for exponential function ($H_p = m_p \bullet SM_p^{n_p}$) at H-pol and V-pol

H-pol		V-pol	
m_H	0.943	m_V	0.874
n_H	0.040	n_V	0.023
R^2	0.626	R^2	0.609

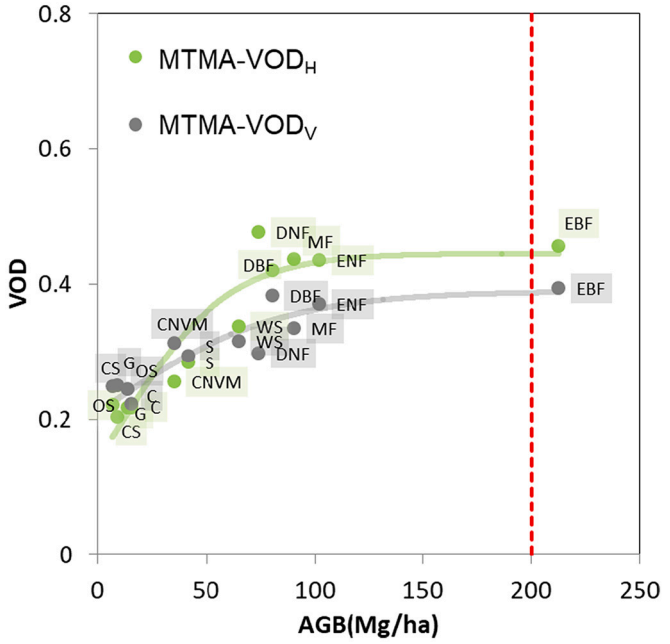

Fig. 15. Comparison between global annual average VOD and AGB of different vegetation types in 2017.

retrievals in these areas were still expected to be improved if we consider adding constraints to the parameters to be retrieved in the cost function. Therefore, although the saturation of VOD_p in dense forest area is a limitation of the MTMA, it is possible to be further improved in future research.

In addition, in this study, only 11 ground validation networks were used to evaluate SM products at the global scale, but the number of networks and their corresponding vegetation types might not be sufficient for a reliable global validation. The fact is that the number of available networks with sufficient observations to support a reliable validation of the large-scale (tens of kilometers) SM retrievals with L-band radiometry is limited. Therefore, more validation sites that covers diverse land cover types especially for dense vegetation areas are needed towards a more comprehensive validation.

6. Conclusion

In this study, we proposed a multi-temporal and multi-angular (namely MTMA) approach to systematically retrieve four parameters of VOD_p, ω_p^{eff}, SM_p and Z_p^s based on the theoretical microwave vegetation indices from H-pol or V-pol SMOS data. The proposed algorithm assumes that vegetation parameters of VOD_p and ω_p^{eff} do not change in temporal adjacent overpasses over short period (i.e. in a couple of days), while soil parameters of SM_p and Z_p^s remain to be time-varying. Through a moving-window retrieval, daily and polarization-dependent results of the four parameters are obtained and compared with the in-situ measurements and other existing SMOS-L3 and SMOS-IC products.

Notably, the vegetation parameters are retrieved in this study based on H-pol and V-pol SMOS TB, respectively. The spatio-temporal

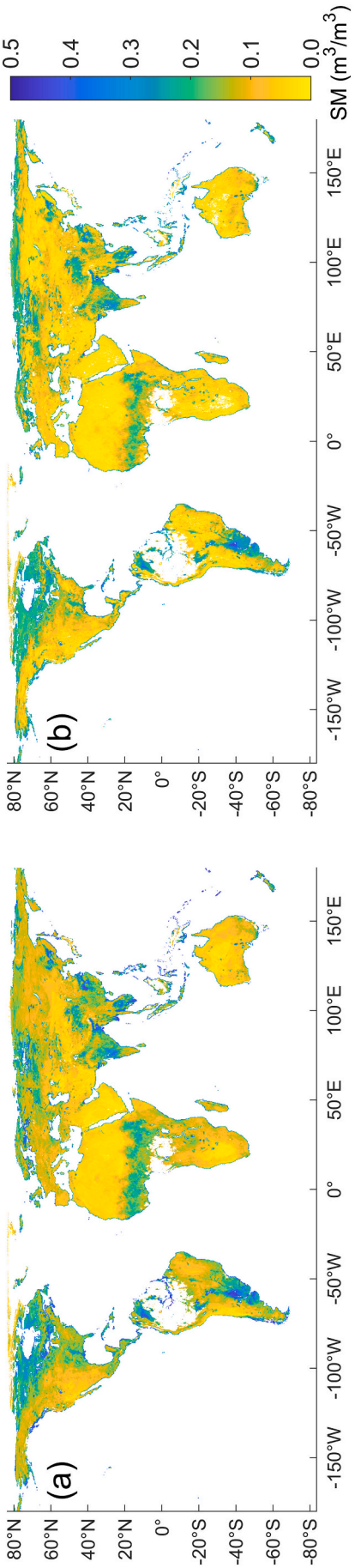

Fig. 16. The global distribution of SM (sm^3/sm^3) after filtering out the values that exceed the threshold based on AGB data: (a) *MTMA-SM$_H$* and (b) *MTMA-SM$_V$*.

distribution of the retrieved VOD by the MTMA is similar to SMOS-L3 and SMOS-IC products. In the dense vegetation area (Amazon forest in South America and Congo forest in Africa), the $MTMA\text{-}VOD_p$ are lower than the other two products due to a saturation of signals in angular dependence of TB. The SMOS-L3 VOD is relatively noisy compared with the other three products, which may be attributed to the error accumulation in the algorithm. The SMOS-IC products have the fewest number of VOD retrievals, which may be due to the strict quality control of the RFI effects, which is modulated in the algorithm using the flag of TB_RMSE (Fernandez-Moran et al., 2017a; Wigneron et al., 2021). The $MTMA\text{-}\omega_H^{eff}$ and $MTMA\text{-}\omega_V^{eff}$ obtained by the proposed MTMA method in this study correspond to the characteristics of vegetation types on a global scale, the values of $MTMA\text{-}\omega_H^{eff}$ and $MTMA\text{-}\omega_V^{eff}$ for low vegetation (grass and savannas) are 0–0.046 and 0–0.122, and the values for high vegetation (forest) are 0.035–0.043 and 0.104–0.138, respectively, indicating a stronger vegetation scattering effects at V-pol. By comparing the differences between H-pol and V-pol vegetation parameters (VOD_p and ω_p^{eff}), it is suggested that attention should be paid to the polarization dependence of vegetation effects in SM retrieval algorithms based on the spaceborne passive microwave remote sensing observations, although it is a very challenging task to validate.

The performance of the MTMA retrieved SM was validated with in-situ measurements from 11 dense networks. The $MTMA\text{-}SM_H$ and $MTMA\text{-}SM_V$ can capture very well the dynamic changes of SM and have a good correlation with the in-situ data (overall $R > 0.75$). The overall ubRMSE for $MTMA\text{-}SM_H$ and $MTMA\text{-}SM_V$ are 0.050 m^3/m^3 and 0.054 m^3/m^3 respectively and are lower than that of SMOS-L3 and SMOS-IC products. However, the SMOS-IC products generally present higher correlation coefficients compared to $MTMA\text{-}SM_H$ in most sites outside China; RFI filtering is crucial in China and makes very difficult to compare different retrieval algorithms based on different TB products. However, The improved results obtained by the MTMA in China strongly suggest that the use of TB refined by the two-step regression approach to filter the RFI is very performant in regions densely affected by RFI. The $MTMA\text{-}SM_H$ and $MTMA\text{-}SM_V$ are lower than SMOS-IC product in dense vegetation areas (tropical forests in Central Africa and Amazon areas) due to a relatively low values of $MTMA\text{-}VOD_H$ and $MTMA\text{-}VOD_V$. The retrieved values of the roughness parameters Z_p^s in this study are relatively high in dense forest area (Amazon forest in South America and Congo forest in Africa) and parts of the Sahara desert in northern Africa, which is consistent with the results from Saleh et al. (2006), Grant et al. (2007) and Pellarin et al. (2009). In addition, it is found that the roughness effects can be dependent on soil moisture even at the satellite pixel/grid scale, indicating the importance of simultaneous retrieval of SM and roughness.

The method proposed in this study takes full advantage of the multi-angular features of SMOS data to decouple the soil-vegetation interactions and makes full use of multi-temporal observations to increase the abundance of information of satellite measurements used in the algorithm for additional retrieval of vegetation effective scattering albedo and soil roughness. The limitation of the algorithm is its large sensitivity to TB variability with incidence angles, resulting in increased uncertainties in dense vegetation areas (AGB above 200 Mg/ha) where the TB variation with incident angle is small, which should be further improved in subsequent research.

Declaration of Competing Interest

The authors declare that they have no known competing financial interests or personal relationships that could have appeared to influence the work reported in this paper.

Acknowledgements

This study was jointly supported by the Strategic Priority Research Program of the Chinese Academy of Sciences (Grant No. XDA19030203), the National Natural Science Foundation of China (NSFC) (Grant no. 42090014) and the Second Tibetan Plateau Scientific Expedition and Research Program (STEP) (Grant No. 2019QZKK0103, 2019QZKK0206). We gratefully thank the Centre Aval de Traitement des Données SMOS and NASA Distributed Active Archive Center for providing satellite products. In-situ SM data are contributed partly by the International Soil Moisture Network (ISMN), partly by Professor Z. Su and K. Yang, and partly by the U.S. Department of Agriculture, Agricultural Research Service. USDA is an equal opportunity provider and employer.

Appendix A. Supplementary data

Supplementary data to this article can be found online at https://doi.org/10.1016/j.rse.2022.113190.

References

Al Bitar, A., Mialon, A., Kerr, Y.H., Cabot, F., Richaume, P., Jacquette, E., Quesney, A., Mahmoodi, A., Tarot, S., Parrens, M., Al-Yaari, A., Pellarin, T., Rodriguez-Fernandez, N., Wigneron, J.-P., 2017. The global SMOS level 3 daily soil moisture and brightness temperature maps. Earth Syst. Sci. Data 9, 293–315.

Al-Yaari, A., Ducharne, A., Cheruy, F., Crow, W.T., Wigneron, J.P., 2019. Satellite-based soil moisture provides missing link between summertime precipitation and surface temperature biases in CMIP5 simulations over conterminous United States. Sci. Rep. 9, 1657.

Baur, M.J., Jagdhuber, T., Feldman, A.F., Akbar, R., Entekhabi, D., 2019. Estimation of relative canopy absorption and scattering at L-, C- and X-bands. Remote Sens. Environ. 233, 111384.

Brandt, M., Wigneron, J.P., Chave, J., Tagesson, T., Penuelas, J., Ciais, P., Rasmussen, K., Tian, F., Mbow, C., Al-Yaari, A., Rodriguez-Fernandez, N., Schurgers, G., Zhang, W., Chang, J., Kerr, Y., Verger, A., Tucker, C., Mialon, A., Rasmussen, L.V., Fan, L., Fensholt, R., 2018. Satellite passive microwaves reveal recent climate-induced carbon losses in African drylands. Nat. Ecol. Evol. 2, 827–835.

Chaubell, M.J., Yueh, S.H., Dunbar, R.S., Colliander, A., Chen, F., Chan, S.K., Entekhabi, D., Bindlish, R., O'Neill, P.E., Asanuma, J., Berg, A.A., Bosch, D.D., Caldwell, T., Cosh, M.H., Holifield Collins, C., Martinez-Fernandez, J., Seyfried, M., Starks, P.J., Su, Z., Thibeault, M., Walker, J., 2020. Improved SMAP dual-channel algorithm for the retrieval of soil moisture. IEEE Trans. Geosci. Remote Sens. 58, 3894–3905.

Chen, Y.Y., Yang, K., Qin, J., Cui, Q., Lu, H., La, Z., Han, M.L., Tang, W.J., 2017. Evaluation of SMAP, SMOS, and AMSR2 soil moisture retrievals against observations from two networks on the Tibetan Plateau. J. Geophys. Res.-Atmos. 122, 5780–5792.

Cui, Q., Shi, J., Du, J., Zhao, T., Xiong, C., 2015. An approach for monitoring global vegetation based on multiangular observations from SMOS. IEEE J. Sel. Top. Appl. Earth Obs. Remote Sens. 8, 604–616.

Davenport, I.J., Fernandez-Galvez, J., Gurney, R.J., 2005. A sensitivity analysis of soil moisture retrieval from the Tau-Omega microwave emission model. IEEE Trans. Geo. Remote Sens. 43, 1304–1316.

Diego, C.D.S.A., Suzana, M.G.L.M., Ana, C.V.E.L.G., Diogo, F.B.R., 2018. Validation of SMOS-IC soil moisture over Brazilian semiarid using in situ measurements. In: 13th International Conference on Hydroinformatics, 3, pp. 54–61.

Ebrahimi-Khusfi, M., Alavipanah, S.K., Hamzeh, S., Amiraslani, F., Neysani Samany, N., Wigneron, J.-P., 2018. Comparison of soil moisture retrieval algorithms based on the synergy between SMAP and SMOS-IC. Int. J. Appl. Earth Obs. Geoinf. 67, 148–160.

Escorihuela, M.J., Kerr, Y.H., Rosnay, P.D., Wigneron, J.P., Calvet, J.C., Lemaitre, F., 2007. A simple model of the bare soil microwave emission at L-band. IEEE Trans. Geosci. Remote Sens. 45, 1978–1987.

Fernandez-Moran, R., Al-Yaari, A., Mialon, A., Mahmoodi, A., Al Bitar, A., De Lannoy, G., Lopez-Baeza, E., Kerr, Y., Wigneron, J.-P., 2017a. SMOS-IC:an alternative SMOS soil moisture and vegetation optical depth product. Remote Sens. 9.

Fernandez-Moran, R., Wigneron, J.P., De Lannoy, G., Lopez-Baeza, E., Parrens, M., Mialon, A., Mahmoodi, A., Al-Yaari, A., Bircher, S., Al Bitar, A., Richaume, P., Kerr, Y., 2017b. A new calibration of the effective scattering albedo and soil roughness parameters in the SMOS SM retrieval algorithm. Int. J. Appl. Earth Obs. Geoinf. 62, 27–38.

Ferrazzoli, P., Guerriero, L., Wigneron, J.P., 2002. Simulating L-band emission of forests in view of future satellite applications. IEEE Trans. Geosci. Remote Sens. 40, 2700–2708.

Gherboudj, I., Magagi, R., Goita, K., Berg, A.A., Toth, B., Walker, A., 2012. Validation of SMOS data over agricultural and boreal forest areas in Canada. IEEE Trans. Geosci. Remote Sens. 50, 1623–1635.

Grant, J.P., Wigneron, J.P., Van de Griend, A.A., Kruszewski, A., Søbjærg, S.S., Skou, N., 2007. A field experiment on microwave forest radiometry: L-band signal behaviour for varying conditions of surface wetness. Remote Sens. Environ. 109, 10–19.

Grant, J.P., Saleh-Contell, K., Wigneron, J.P., Guglielmetti, M., Kerr, Y.H., Schwank, M., Skou, N., Van de Griend, A.A., 2008. Calibration of the L-MEB model over a coniferous and a deciduous forest. IEEE Trans. Geosci. Remote Sens. 46, 808–818.

Grant, J.P., Wigneron, J.-P., Drusch, M., Williams, M., Law, B.E., Novello, N., Kerr, Y., 2012. Investigating temporal variations in vegetation water content derived from SMOS optical depth. In: IGARSS 2012.

Griend, A.A.V.D., Owe, M., 1994. Microwave vegetation optical depth and inverse modelling of soil emissivity using Nimbus/SMMR satellite observations. Meteorol. Atmos. Phys. 54, 225–239.
Jackson, T.J., Schmugge, T.J., 1991. Vegetation effects on the microwave emission of soils. Remote Sens. Environ. 36, 203–212.
Jackson, T., Chen, D., Cosh, M., 2004. Vegetation water content mapping using Landsat data derived normalized difference water index for corn and soybeans. Remote Sens. Environ. 92, 475–482.
Jackson, T.J., Bindlish, R., Cosh, M.H., Zhao, T.J., Starks, P.J., Bosch, D.D., Seyfried, M., Moran, M.S., Goodrich, D.C., Kerr, Y.H., Leroux, D., 2012. Validation of soil moisture and ocean salinity (SMOS) soil moisture over watershed networks in the U.S. IEEE Trans. Geosci. Remote Sens. 50, 1530–1543.
Kerr, Y.H., Waldteufel, P., Wigneron, J.P., Martinuzzi, J., Font, J., Berger, M., 2001. Soil moisture retrieval from space: the soil moisture and ocean salinity (SMOS) mission. IEEE Trans. Geosci. Remote Sens. Geosci. Remote Sens. 39, 1729–1735.
Kerr, Y.H., Waldteufel, P., Richaume, P., Wigneron, J.P., Ferrazzoli, P., Mahmoodi, A., Al Bitar, A., Cabot, F., Gruhier, C., Juglea, S.E., Leroux, D., Mialon, A., Delwart, S., 2012. The SMOS soil moisture retrieval algorithm. IEEE Trans. Geosci. Remote Sens. 50, 1384–1403.
Kilic, L., Prigent, C., Aires, F., Boutin, J., Heygster, G., Tonboe, R.T., Roquet, H., Jimenez, C., Donlon, C., 2018. Expected performances of the copernicus imaging microwave radiometer (CIMR) for an all-weather and high spatial resolution estimation of ocean and sea ice parameters. J. Geophys. Res. Oceans 123, 7564–7580.
Konings, A.G., Piles, M., Rötzer, K., McColl, K.A., Chan, S.K., Entekhabi, D., 2016. Vegetation optical depth and scattering albedo retrieval using time series of dual-polarized L-band radiometer observations. Remote Sens. Environ. 172, 178–189.
Konings, A.G., Piles, M., Das, N., Entekhabi, D., 2017. L-band vegetation optical depth and effective scattering albedo estimation from SMAP. Remote Sens. Environ. 198, 460–470.
Konings, A.G., Saatchi, S.S., Frankenberg, C., Keller, M., Leshyk, V., Anderegg, W.R.L., Humphrey, V., Matheny, A.M., Trugman, A., Sack, L., Agee, E., Barnes, M.L., Binks, O., Cawse-Nicholson, K., Christoffersen, B.O., Entekhabi, D., Gentine, P., Holtzman, N.M., Katul, G.G., Liu, Y., Longo, M., Martinez-Vilalta, J., McDowell, N., Meir, P., Mencuccini, M., Mrad, A., Novick, K.A., Oliveira, R.S., Siqueira, P., Steele-Dunne, S.C., Thompson, D.R., Wang, Y., Wehr, R., Wood, J.D., Xu, X., Zuidema, P.A., 2021. Detecting forest response to droughts with global observations of vegetation water content. Glob. Chang. Biol. 27, 6005–6024.
Kurum, M., 2013. Quantifying scattering albedo in microwave emission of vegetated terrain. Remote Sens. Environ. 129, 66–74.
Lawrence, H., Wigneron, J.-P., Demontoux, F., Mialon, A., Kerr, Y.H., 2013. Evaluating the semiempirical H–Q model used to calculate the L-band emissivity of a rough bare soil. IEEE Trans. Geosci. Remote Sens. 51, 4075–4084.
Lawrence, H., Wigneron, J.-P., Richaume, P., Novello, N., Grant, J., Mialon, A., Al Bitar, A., Merlin, O., Guyon, D., Leroux, D., Bircher, S., Kerr, Y., 2014. Comparison between SMOS vegetation optical depth products and MODIS vegetation indices over crop zones of the USA. Remote Sens. Environ. 140, 396–406.
Li, X., Al-Yaari, A., Schwank, M., Fan, L., Frappart, F., Swenson, J., Wigneron, J.P., 2020. Compared performances of SMOS-IC soil moisture and vegetation optical depth retrievals based on tau-omega and two-stream microwave emission models. Remote Sens. Environ. 236, 111502.
Li, X., Wigneron, J.-P., Frappart, F., Fan, L., Ciais, P., Fensholt, R., Entekhabi, D., Brandt, M., Konings, A.G., Liu, X., Wang, M., Al-Yaari, A., Moisy, C., 2021a. Global-scale assessment and inter-comparison of recently developed/reprocessed microwave satellite vegetation optical depth products. Remote Sens. Environ. 253, 112208.
Li, X., Wigneron, J.P., Frappart, F., Fan, L., Moisy, C., 2021b. Global-Scale Assessment and Inter-Comparison of Recently Developed/Reprocessed Microwave Satellite Vegetation Optical Depth Products.
Li, X., Wigneron, J.-P., Fan, L., Frappart, F., Yueh, S.H., Colliander, A., Ebtehaj, A., Gao, L., Fernandez-Moran, R., Liu, X., Wang, M., Ma, H., Moisy, C., Ciais, P., 2022. A new SMAP soil moisture and vegetation optical depth product (SMAP-IB): algorithm, assessment and inter-comparison. Remote Sens. Environ. 271, 112921.
Liu, J., Chai, L., Lu, Z., Liu, S., Qu, Y., Geng, D., Song, Y., Guan, Y., Guo, Z., Wang, J., Zhu, Z., 2019. Evaluation of SMAP, SMOS-IC, FY3B, JAXA, and LPRM soil moisture products over the Qinghai-Tibet plateau and its surrounding areas. Remote Sens. 11, 792.
Mironov, V.L., Kosolapova, L.G., Fomin, S.V., 2009. Physically and mineralogically based spectroscopic dielectric model for moist soils. IEEE Trans. Geosci. Remote Sens. 47, 2059–2070.
Mo, T., Choudhury, B.J., Schmugge, T.J., Wang, J.R., Jackson, T.J., 1982. A model for microwave emission from vegetation-covered fields. J. Geophys. Res. 87, 11229.
Montpetit, B., Royer, A., Wigneron, J.P., Chanzy, A., Mialon, A., 2015. Evaluation of multi-frequency bare soil microwave reflectivity models. Remote Sens. Environ. 162, 186–195.
Parrens, M., Wigneron, J.-P., Richaume, P., Mialon, A., Al Bitar, A., Fernandez-Moran, R., Al-Yaari, A., Kerr, Y.H., 2016. Global-scale surface roughness effects at L-band as estimated from SMOS observations. Remote Sens. Environ. 181, 122–136.
Pellarin, T., Tran, T., Cohard, J.M., Galle, S., Laurent, J.P., de Rosnay, P., Vischel, T., 2009. Soil moisture mapping over West Africa with a 30-min temporal resolution using AMSR-E observations and a satellite-based rainfall product. Hydrol. Earth Syst. Sci. 13, 1887–1896.
Peng, J., Niesel, J., Loew, A., Zhang, S., Wang, J., 2015. Evaluation of satellite and reanalysis soil moisture products over Southwest China using ground-based measurements. Remote Sens. 7, 15729–15747.
Peng, B., Zhao, T., Shi, J., Lu, H., Mialon, A., Kerr, Y.H., Liang, X., Guan, K., 2017. Reappraisal of the roughness effect parameterization schemes for L-band radiometry over bare soil. Remote Sens. Environ. 199, 63–77.
Rodríguez-Fernández, N.J., Mialon, A., Mermoz, S., Bouvet, A., Richaume, P., Al Bitar, A., Al-Yaari, A., Brandt, M., Kaminski, T., Le Toan, T., Kerr, Y.H., Wigneron, J.-P., 2018. An evaluation of SMOS L-band vegetation optical depth (L-VOD) data sets: high sensitivity of L-VOD to above-ground biomass in Africa. Biogeosciences 15, 4627–4645.
Saleh, K., Wigneron, J.-P., de Rosnay, P., Calvet, J.-C., Kerr, Y., 2006. Semi-empirical regressions at L-band applied to surface soil moisture retrievals over grass. Remote Sens. Environ. 101, 415–426.
Schlenz, F., Dall'amico, J.T., Mauser, W., Loew, A., 2012. Analysis of SMOS brightness temperature and vegetation optical depth data with coupled land surface and radiative transfer models in Southern Germany. Hydrol. Earth Syst. Sci. 16, 3517–3533.
Schneeberger, K., Schwank, M., Stamm, C., Rosnay, P.D., Mtzler, C., Flühler, H., 2004. Topsoil structure influencing soil water retrieval by microwave radiometry. Vadose Zone J. 3.
Seneviratne, S.I., Corti, T., Davin, E.L., Hirschi, M., Jaeger, E.B., Lehner, I., Orlowsky, B., Teuling, A.J., 2010. Investigating soil moisture–climate interactions in a changing climate: a review. Earth Sci. Rev. 99, 125–161.
Shi, J., Jackson, T., Tao, J., Du, J., Bindlish, R., Lu, L., Chen, K.S., 2008. Microwave vegetation indices for short vegetation covers from satellite passive microwave sensor AMSR-E. Remote Sens. Environ. 112, 4285–4300.
Shi, J., Zhao, T., Cui, Q., Yao, P., 2019. Airborne and Spaceborne Passive Microwave Measurements of Soil Moisture, 2, pp. 71–105.
Tian, F., Wigneron, J.-P., Ciais, P., Chave, J., Ogee, J., Penuelas, J., Raebild, A., Domec, J. C., Tong, X., Brandt, M., Mialon, A., Rodriguez-Fernandez, N., Tagesson, T., Al-Yaari, A., Kerr, Y., Chen, C., Myneni, R.B., Zhang, W., Ardo, J., Fensholt, R., 2018. Coupling of ecosystem-scale plant water storage and leaf phenology observed by satellite. Nat. Ecol. Evol. 2, 1428–1435.
Wang, M., Fan, L., Frappart, F., Ciais, P., Sun, R., Liu, Y., Li, X., Liu, X., Moisy, C., Wigneron, J.-P., 2021. An alternative AMSR2 vegetation optical depth for monitoring vegetation at large scales. Remote Sens. Environ. 263, 112556.
Wigneron, J.P., Chanzy, A., Calvet, J.C., Bruguier, N., 1995. A simple algorithm to retrieve soil moisture and vegetation biomass using passive microwave measurements over crop fields. Remote Sens. Environ. 51, 331–341.
Wigneron, J.-P., Waldteufel, P., Chanzy, A., Calvet, J.C., Kerr, Y.H., 2000. Two-dimensional microwave interferometer retrieval capabilities over land surfaces (SMOS mission). Remote Sens. Environ. 112, 4285–4300.
Wigneron, J.P., Laguerre, L., Kerr, Y.H., 2001. A simple parameterization of the L-band microwave emission from rough agricultural soils. IEEE Trans. Geosci. Remote Sens. 39, 1697–1707.
Wigneron, J.-P., Pardé, M., Waldteufel, P., Chanzy, A., Skou, N., 2004a. Characterizing the dependence of vegetation model parameters on crop structure, incidence angle, and polarization at L-band. Geo Remote Sens. IEEE Trans. 42, 416–425.
Wigneron, J.P., Pardé, M., Waldteufel, P., Chanzy, A., Skou, N., 2004b. Characterizing the dependence of vegetation model parameters on crop structure, incidence angle, and polarization at L-band. Geosci. Remote Sens. IEEE Trans. 42, 416–425.
Wigneron, J.-P., Kerr, Y., Waldteufel, P., Saleh, K., Escorihuela, M.J., Richaume, P., Ferrazzoli, P., Rosnay, P.D., Gurney, R., Calvet, J.C., 2007. L-band microwave emission of the biosphere (L-MEB) model: description and calibration against experimental data sets over crop fields. Remote Sens. Environ. 107, 639–655.
Wigneron, J.-P., Chanzy, A., Kerr, Y.H., Lawrence, H., Shi, J., Escorihuela, M.J., Mironov, V., Mialon, A., Demontoux, F., de Rosnay, P., Saleh-Contell, K., 2011. Evaluating an improved parameterization of the soil emission in L-MEB. IEEE Trans. Geosci. Remote Sens. 49, 1177–1189.
Wigneron, J.-P., Jackson, T.J., O'Neill, P., De Lannoy, G., de Rosnay, P., Walker, J.P., Ferrazzoli, P., Mironov, V., Bircher, S., Grant, J.P., Kurum, M., Schwank, M., Munoz-Sabater, J., Das, N., Royer, A., Al-Yaari, A., Al Bitar, A., Fernandez-Moran, R., Lawrence, H., Mialon, A., Parrens, M., Richaume, P., Delwart, S., Kerr, Y.H., 2017. Modelling the passive microwave signature from land surfaces: a review of recent results and application to the L-band SMOS & SMAP soil moisture retrieval algorithms. Remote Sens. Environ. 192, 238–262.
Wigneron, J.-P., Li, X., Frappart, F., Fan, L., Al-Yaari, A., De Lannoy, G., Liu, X., Wang, M., Le Masson, E., Moisy, C., 2021. SMOS-IC data record of soil moisture and L-VOD: historical development, applications and perspectives. Remote Sens. Environ. 254, 112238.
Zhao, T., 2018. Recent advances of L-band application in the passive microwave remote sensing of soil moisture and its prospects. Prog. Geogr. 37, 198–213.
Zhao, T., Shi, J., Bindlish, R., Jackson, T., Cosh, M., Jiang, L., Zhang, Z., Lan, H., 2015a. Parametric exponentially correlated surface emission model for L-band passive microwave soil moisture retrieval. Phys. Chem. Earth Parts A/B/C 83-84, 65–74.
Zhao, T., Shi, J., Bindlish, R., Jackson, T.J., Kerr, Y.H., Cosh, M.H., Cui, Q., Li, Y., Xiong, C., Che, T., 2015b. Refinement of SMOS multiangular brightness temperature toward soil moisture retrieval and its analysis over reference targets. IEEE J. Sel. Top. Appl. Earth Obs. Remote Sens. 8, 589–603.

Zhao, T., Hu, L., Shi, J., Lü, H., Li, S., Fan, D., Wang, P., Geng, D., Kang, C.S., Zhang, Z., 2020a. Soil moisture retrievals using L-band radiometry from variable angular ground-based and airborne observations. Remote Sens. Environ. 248, 111958.
Zhao, T., Shi, J., Lv, L., Xu, H., Chen, D., Cui, Q., Jackson, T.J., Yan, G., Jia, L., Chen, L., Zhao, K., Zheng, X., Zhao, L., Zheng, C., Ji, D., Xiong, C., Wang, T., Li, R., Pan, J., Wen, J., Yu, C., Zheng, Y., Jiang, L., Chai, L., Lu, H., Yao, P., Ma, J., Lv, H., Wu, J., Zhao, W., Yang, N., Guo, P., Li, Y., Hu, L., Geng, D., Zhang, Z., 2020b. Soil moisture experiment in the Luan River supporting new satellite mission opportunities. Remote Sens. Environ. 240, 111680.
Zhao, T., Shi, J., Entekhabi, D., Jackson, T.J., Hu, L., Peng, Z., Yao, P., Li, S., Kang, C.S., 2021. Retrievals of soil moisture and vegetation optical depth using a multi-channel collaborative algorithm. Remote Sens. Environ. 257, 112321.